

# Core-dictated tuning of the performance of amorphous and crystalline TM@Pt and HEA@Pt core-shell nanoparticles catalysts

Ilya V. Chepkasov <sup>a,b</sup>, Viktor S. Baidyshev <sup>a</sup>, Alexander G. Kvashnin <sup>a</sup>

<sup>a</sup> Skolkovo Institute of Science and Technology, Bolshoy Boulevard 30, bld. 1, Moscow 121205, Russian Federation

<sup>b</sup> Katanov Khakass State University, 90 Lenin pr., 655017, Abakan, Russian Federation

## ARTICLE INFO

### Keywords:

Core-shell nanoparticles

Amorphous

Crystalline

High-entropy alloy

## ABSTRACT

This study employs density functional theory (DFT) to investigate how the composition (individual metals: Ag, Au, Cu, Ir, Pd, Rh, Ru; or high-entropy alloy, HEA = AgAuCuIrPdRhRu) and structure (crystalline fcc vs. amorphous) of the core in Pt-shell nanoparticles dictates their catalytic properties. Core-induced effects of electronic charge redistribution, lattice strain, and shifts in the *d*-band center of surface Pt atoms collectively tune adsorption energies for key molecules (CO, NO, CH<sub>3</sub> and NH<sub>3</sub>). Low-work-function cores (Ag, Cu, Ru) enrich electron density on Pt surfaces, favoring the adsorption of electron acceptors. Compressive strain from lattice-mismatched cores, such as Cu, downshifts the *d*-band center, weakening the binding of adsorbates. Amorphous structures exhibit broad, quasi-continuous adsorption energy distributions due to a large variety of surface sites, contrasting with the discrete peaks observed for ordered fcc nanoparticles. HEA cores uniquely change strain and electron distribution across the nanoparticle structure to a smoother one in both structural states, creating multiple inequivalent active sites. Reducing the Pt shell thickness amplifies charge transfer and strain, particularly for low-work-function cores, while HEA cores enhances surface electron density as the shell becomes thinner. Scaling relations (e.g., CH<sub>3</sub> vs. C adsorption) hold for top sites in fcc structures but fail for hollow sites due to multicenter bonding. These insights establish dual-parameter control (core composition/size and crystallinity) to optimize Pt-shell catalysts, highlighting HEA cores and amorphous structures as promising strategies to minimize Pt usage while enhancing reactivity and stability for catalytic applications.

## 1. Introduction

Catalytic materials containing an atomically thin Pt surface layer are promising alternatives to pure Pt nanoparticle catalysts for the oxygen reduction reaction (ORR) [1–3], hydrogen evolution reaction (HER) [4], methanol oxidation reaction [5], emission control catalysts with CO oxidation and NO<sub>x</sub> decomposition reactions [6,7] and et al. [8–12]. Pt-shelled catalysts can be stable with significantly less Pt loading than commercial alternatives, and they can show higher activity [13–20]. Core–shell nanoparticles compared to alloys, have specific lattice strains and ligand effects that tailor their geometric and electronic properties [21–32]. The catalytic activity of such a core–shell catalyst depends on the synergistic interactions between the core and the shell [33]. There are three main effects that can determine the catalytic activity of core–shell materials [34], namely (i) the ligand effect, which refers to the interaction between the core and the shell, (ii) the ensemble effect, which is governed by the adsorption of the material on the surface and (iii) the geometric effects [5,35]. These three factors can significantly interfere with and affect the overall reactivity.

This is particularly the case for lattice strains, which typically exhibit significant modulation of the electronic properties of the shell and the corresponding reactivity [35–40].

Changing the core composition of Pt-shell particles may lead to significant changes in their ORR activity [41]. In particular, Zhang and Henkelman [16] showed that the core made of Pd, Cu, Ir, Rh and Ru leads to a reduction in the oxygen binding energy of the Pt shell, when they are located within the core. However, Au and Ag increase the oxygen binding energy. The target value of oxygen binding can be achieved by alloying metals in core and the peak of activity is achieved for a Au<sub>28</sub>Pd<sub>72</sub>@Pt nanoparticles [16]. It was also shown by Zhang and Henkelman [17] that the predicted reaction rate for CO oxidation on Au<sub>0.65</sub>Pd<sub>0.35</sub>@Pt and Au<sub>0.73</sub>Pt<sub>0.27</sub>@Pt nanoparticles could be 200 times higher than on Pt(111) [17]. In addition to the effect of the core structure, the thickness of the Pt shell also affects the properties of core–shell catalysts [42]. The optimum number of Pt layers required to obtain the best performance may vary for different catalysts, depending on the properties of the cores. For example, Wu

\* Corresponding author at: Skolkovo Institute of Science and Technology, Bolshoy Boulevard 30, bld. 1, Moscow 121205, Russian Federation.  
E-mail address: [I.Chepkasov@skoltech.ru](mailto:I.Chepkasov@skoltech.ru) (I.V. Chepkasov).

et al. [43] systematically investigated the effects of Pt layer thickness on the ORR activity of Pt-shell catalysts using DFT calculations. The study examined different metals within the core, such as V, Cr, Fe, Co, Ni, Cu. It has been shown that the binding energy of oxygen decreases with an increasing number of platinum shells, which leads to improved performance of catalysts. The system with three Pt-layers was found to have better ORR activity than one- or two-layer catalysts.

Recent advances in catalysis have been driven by high-entropy alloys (HEAs) [44]. These materials, comprising five or more principal elements while retaining the specific crystal structure of their parent binary intermetallic [45–47], offer broader compositional tunability than binary or ternary intermetallics. Furthermore, their unique structural stability derived from sluggish diffusion and high-entropy effects [48–50], represents a key advantage in tuning of the catalytic properties. Extending low-platinum intermetallic materials to high-entropy alloys (HEA) could enable the discovery of more efficient catalysts for oxygen reduction [51]. However, designing HEA compositions remains a formidable challenge due to the vast elemental and stoichiometric configurational space, which makes traditional trial-and-error approaches impractical. Recently, machine learning (ML) has significantly accelerated the screening and discovery of high-performance catalysts [52–54]. Omidvar et al. [55] used the TinNet [56] interpretable framework combined with an active learning approach to accelerate the discovery of Pt monolayer core–shell catalysts for ORR. Through high-throughput screening of 17,000 candidate structures and active learning, TinNet identifies novel alloys and confirms known systems in the reactivity “goldilocks zone” using OH adsorption energy as a key descriptor. Their findings highlight the potential of modulating active sites through core–shell alloying and incorporating buffer layers of Ir, Rh, and Ru, offering a promising strategy to enhance surface reactivity and reduce Pt usage for the ORR. Zhang et al. [57] employ a machine learning-guided strategy using crystal graph convolutional neural networks (CGCNN) to accelerate the discovery of low-platinum high-entropy intermetallic materials for the oxygen reduction reaction in fuel cells. During the ML search, FeCoNiCu@Pt was identified as the most promising composition for the ORR catalyst. The experimentally synthesized FeCoNiCu@Pt/C nanocatalyst exhibited ultra-high mass activity and specific activity. In addition, the catalyst exhibited significantly improved electrochemical stability, which can be attributed to the slow diffusion effect in the HEA structure [57]. Also, such HEA-core Pt-shell structures are more stable and less prone to sintering. In particular, Pan et al. [58] introduced an “entropy-increase assisted anti-sintering” strategy to synthesize high-loaded (40.53 wt%) platinum high-entropy intermetallic materials with ultrafine particle size on carbon supports for proton exchange membrane fuel cells. By increasing the configurational entropy of precursor alloys the surface energy of nanoparticles is reduced, fundamentally suppressing sintering during high-temperature ordering treatments. The resulting Pt-HEA@Pt/C catalyst exhibited exceptional ORR mass activity and durability (only 12.5% decay after 30,000 cycles). DFT calculations revealed that the compressive strain from the HEA core optimizes \*OOH adsorption on the Pt shell, elevating the energy barrier for Pt dissolution and simultaneously enhancing intrinsic activity and stability [58].

One of the ways to improve nanocatalysts could be amorphization of the structure. For example, for the alkaline HER process, surface reconstruction is a frequently observed phenomenon and usually leads to the formation of an amorphous layer [59,60]. However, the fundamental understanding of the surface amorphization process and the role of the resulting amorphous layer in catalysts is still debated. Additionally, how to effectively utilize the inevitably amorphous layers and further improve the catalytic activity of electrocatalytic materials remains a challenging task [61]. Compared to the most studied crystalline nanomaterials, amorphous catalysts possess unique chemical ordering, structural flexibility at the atomic level, and an abundance of defects [62–65,65]. Due to these unique features, such as amorphous

structural and chemical disorder, amorphous catalysts can be fully active compared to their crystalline counterparts, which are only surface active. Rich defects and dangling bonds effectively enhance the intrinsic activity and electrochemical stability of amorphous catalysts [66].

Previously, a large number of works have been published devoted to the theoretical and experimental studies of the tuning properties of Pt-shell nanocatalysts. All these works considered only crystalline structures [16,42,67–73]. In this paper we investigated the effect of the structure on the adsorption properties of transition metal@Pt and HEA@Pt core–shell nanoparticles with fcc and amorphous structures. We selected 7 transition metals as cores - Ag, Au, Cu, Ir, Pd, Rh, Ru and 7-component HEA was made from these metals (HEA=AgAuCuIrPdRhRu). The review of Huang et al. [74] highlighted the outstanding electrocatalytic performance of noble-metal-based HEA NPs. This performance stems from the superior electronic properties of noble metals, combined with the inherent stability of HEAs provided by their sluggish atomic kinetics and high mixing entropy, which allows them to endure harsh reaction conditions [75,76]. HEA nanoparticles made from these transition metals are actively synthesized and studied experimentally such as AuAgPtPdCu (CO<sub>2</sub>RR) [77], IrPdPtRhRu (HER) [78], PtAuPdRhRu (HER) [79], RuRhPdIrPt (ORR) [80], PtRhPdIrRu (HER, GOR, HOR, MOR, EOR) [81], PtRhPdIrRu (HER, HOR) [82], PdPtRuRhAu (OER) [83], IrPdPtRhRu (HER) [75], IrPdPtRhRu (HER) [84], PdPtRuRhAu (HER) [85], RuRhIrPtPd (HER) [86], disordered-PtRhPdIrRu (HER, HOR) [82] and theoretically such as AgAuCuIr-PdPtRhRu (ORR) [87], AgIrPdPtRu [88], IrPdPtRhRu (ORR) [89], IrPdPtRhRu (HER) [90] for catalytic applications [76,91]. Nanoparticles consisting of a HEA core and a Pt shell (HEA@Pt [57,58,92–95]) are also attracting increasing interest due to their promising catalytic properties.

## 2. Methods

To analyze the electronic structure and surface charge of nanoparticles using density functional theory (DFT) [96,97], we first optimize the geometry of each studied nanoparticle. The Generalized Gradient Approximation (GGA) is used with the revised PBE [98] parametrization for the exchange–correlation functional as implemented in the VASP software package [99–101]. The ion-electron interaction is described by the projector-augmented-wave (PAW) method [102] with a cut-off energy of 480 eV. The orbital occupancies are smeared using the first-order Methfessel-Paxton method with a smearing width of 0.05 eV. The local geometry optimization of the considered clusters is performed until the maximum force on each atom becomes less than 0.03 eV/Å. The nanoparticles are placed in a box with a vacuum of at least 10 Å separating them.

The spin-polarized Generalized Gradient Approximation (GGA) with the PBE parametrization is used to calculate the adsorption energies. The Grimme correction (DFT-D3) [103] is applied to account for the dispersive van der Waals interaction. The results of the calculations are post-processed and visualized using the Open Visualization Tool (OVITO) [104] and the VESTA package [105,106]. Electron transfer is studied using the Bader analysis [107]. To determine the structural stability, the excess energy [108] of nanoparticles with respect to a bulk is calculated as follows:

$$\Delta = (E_{NP_s} - \sum_{i=1}^7 E_i N_i) / (\sum_{i=1}^7 N_i)^{2/3}, \quad (1)$$

where  $E_{NP_s}$  is the energy of the considered nanoparticle,  $N_i$  corresponds to the number of individual metals in the nanoparticles, index  $i$  denotes the sequence number of metal atoms, and  $E_i$  are the energies per atom for the individual bulk metals.

The adsorption energies of CO, NO, CH<sub>3</sub>, and NH<sub>3</sub> are calculated using the following formula:

$$E_{ads}[A] = E[A/NP] - E[NP] - E[A], \quad (2)$$

where  $E[A/NP]$  are the energies of adsorption of a complex A = CO, NO, CH<sub>3</sub>, and NH<sub>3</sub> on TM/HEA@Pt (NP) nanoparticles,  $E[NP]$  is the energy of the considered TM/HEA@Pt nanoparticles,  $E[A]$  is the energy of the gas phase CO, NO, CH<sub>3</sub>, and NH<sub>3</sub> molecules.

The Crystal Orbital Hamilton Population (COHP) method is used to investigate the chemical bonding between metallic HEA nanoparticles and adsorbed molecules. In order to extract information about chemical bonding from the electronic density of states (DOS) of a nanoparticle, the crystal orbital overlap population (COOP) is calculated.

COOPs are obtained by multiplying the DOS by the number of overlaps (population). This allows the total electron density to be separated into bonding and anti-bonding states. Consequently, the theory of crystal orbital Hamilton populations (COHP) has been proposed, which generates populations of overlapping orbitals. The sign of COHP is opposite to that of COOP in the case of bonding and anti-bonding states. Therefore -COHP diagrams are always constructed for clarity. The COHP provides a straightforward method of obtaining data on the bonding and anti-bonding states. The mathematical representation of the COHP bears a striking resemblance to a projected DOS equation, but with the density of state matrix weighted by the Hamiltonian matrix elements. In the case of periodic crystals, the COHP can be defined as follows [109]:

$$COHP_{AB}(\epsilon) = \sum_{\nu \in A} \sum_{\mu \in B} COHP_{\mu\nu}(\epsilon) \quad (3)$$

$$COHP_{\mu\nu}(\epsilon) = \frac{2}{V_{BZ}} \int_{BZ} H_{\mu\nu}(k) \left\{ \sum_j c_{\mu j}^*(k) c_{\nu j}(k) \delta(\epsilon - \epsilon_j)(k) \right\} dk \quad (4)$$

where  $H_{\mu\nu}(k)$  is the Hamiltonian matrix in reciprocal space,  $c_{\mu j}(k)$  are the expansion coefficients of the  $j$ th occupied crystal orbital with the energy  $\epsilon_j(k)$  in terms of Bloch functions numbered in the same way as atomic orbitals by the subscript  $\mu$  or  $\nu$ . Integration over  $k$  in the Eq. (4) is performed in the Brillouin zone ( $BZ$ ) with the volume  $V_{BZ}$ .

The negative and positive COHP values, respectively indicating bonding and anti-bonding interactions, result from the weighting of the elements of the Hamiltonian matrix. Integration of COHP up to the Fermi level ( $E_F$ ) gives integrated COHP (ICOHP) values.

$$ICOHP_{AB} = \int_{E_F} COHP_{AB}(\epsilon) d\epsilon \quad (5)$$

All COHP calculations were conducted using the LOBSTER algorithm [110], and further analysis of the contribution of each orbital to the total binding energy was performed using the Dragon software package.

### 3. Results and discussion

Our study is devoted to the identification of distinctive features associated with the influence of the core composition and structure of nanoparticles with a Pt shell on their surface properties, including adsorption properties. A number of transition metals, namely Ag, Au, Cu, Ir, Pd, Rh, and Ru, together with a high-entropy alloy made from these metals (AgAuCuIrPdRhRu) are considered as the core, see Fig. 1a. Here we consider nanoparticles with both fcc and amorphous structure, see Fig. 1a. Amorphous nanoparticles are obtained by molecular dynamics simulation of the melting of fcc nanoparticles with rapid freezing of an amorphous structure (see Online Supplementary material). The investigation focuses on three distinct sizes of nanoparticles, namely 1 nanometer (79 atoms), 1.5 nanometers (201 atoms), and 2 nanometers (321 atoms), Fig. 1b. For 1 nm (79 atoms) core-shell nanoparticles, the core contains 19 atoms in the core (either TM or HEA), and the shell contains 60 Pt atoms with both fcc and amorphous structures. For nanoparticles with a diameter of 1.5 nm (201 atoms) and 2 nm (321 atoms), the size of the core and shell is varied in order to study the effect of the size on the surface properties. We selected 5 cases for core-shell nanoparticles containing 13, 19, 43, 55, 79 atoms in the TM/HEA core, and 188, 182, 158, 146, and 122 Pt shell atoms for nanoparticles

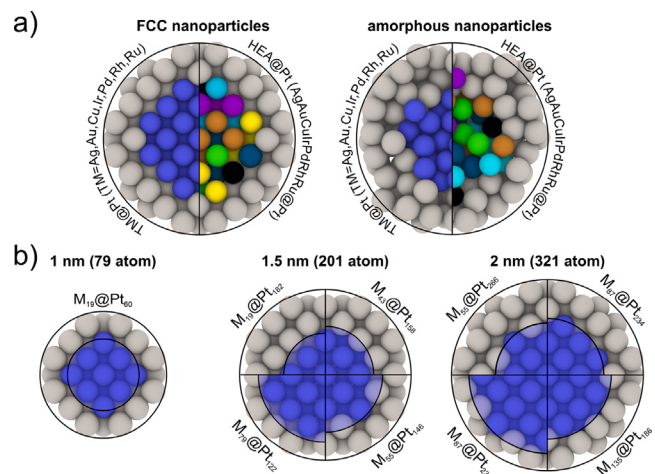


**Fig. 1.** Atomic structures of TM@Pt and HEA@Pt nanoparticles. (a) Slice of 2 nm nanoparticle (321 atom) showing the different core types including different transition metals, namely Ag, Au, Cu, Ir, Pd, Rh, and Ru and HEA made from these metals with fcc and amorphous structures. (b) Slices of nanoparticles of different sizes 1, 1.5, and 2 nm with different sizes of the core highlighted by circles.

of size 1.5 nm, Fig. 1b. It is selected 4 cases for nanoparticles with size of 2 nm, containing 55, 87, 135 and 177 atoms in TM/HEA core and 266, 234, 186 and 144 Pt atoms in the shell, Fig. 1b. More detailed information about structure of considered nanoparticles is shown in Figures S3, S4 in the Online Supplementary material.

#### 3.1. Excess energy

First, we study the stability of nanoparticles with transition metal (TM) of high-entropy (HEA) core and Pt shell. To do this, we calculate  $\Delta$ , which represents the excess energy of the cluster compared to a bulk fragment with the same number of atoms, divided approximately by the number of surface atoms in the cluster, see Eq. (1). The lower the excess energy, the more stable the nanoparticle. The dependence of  $\Delta$  on the core composition of 1 nm nanoparticles with both fcc and amorphous structures is shown in Fig. 2. Amorphous nanoparticles have slightly higher excess energy ( $\Delta$ ) compared to fcc due to the disordered structure and different chemical ordering, but the trends observed are the same. The most stable composition among considered contains copper core (Cu@Pt). Changes in the stability of nanoparticles with respect to core–shell ratio is also calculated for 1.5 nm nanoparticles with fcc and amorphous structure are shown in Fig. S5 in the Online Supplementary material. In the case of Ag@Pt, Cu@Pt, Pd@Pt and Rh@Pt nanoparticles, increasing the core size while simultaneously decreasing the shell size makes them more stable. This indicates that, in experimental synthesis, the formation of a thin Pt shell layer on the core of Ag, Cu, Pd or Rh is more likely than the formation of thick Pt shell layers on the cores of Ag, Cu, Pd or Rh. In other cases, an increase in the core size and a decrease in the shell size does not result in a significant reduction in the  $\Delta$ . However, generally, decreasing the thickness of the Pt shell does not result in a reduction in the stability of core–shell nanoparticles.

#### 3.2. d-band center

To evaluate nanoparticle catalytic efficacy without direct adsorption calculations, computational models can predict reactivity [111,112]. The d-band model developed by Hammer and Nørskov [111] correlates transition metal reactivity with the energy center of surface atoms' d-states. This approach accurately quantifies adsorption energy variations

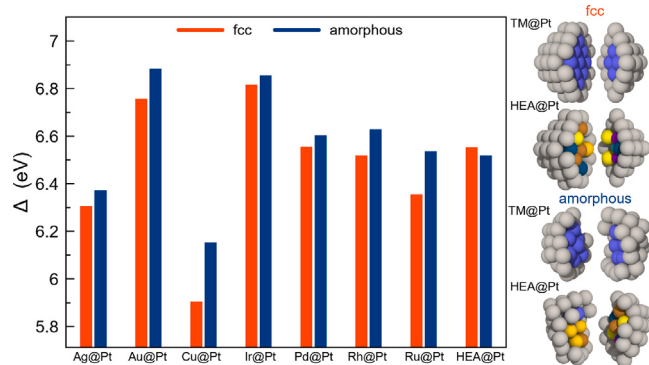


**Fig. 2.** Excess energies  $\Delta$  of TM@Pt and HEA@Pt nanoparticles with 1 nm diameter (79 atoms) with fcc (red bars) and amorphous (blue bars) structure depending on the core composition.

for atomic and molecular species across different nanoparticle surface sites [113]. For all considered core-shell nanoparticles, the  $d$ -band centers are determined by calculating the electronic densities of states projected (pDOS) onto each surface atom. To show how changes in the core composition affect the electronic properties of the Pt atom in the shell, we calculate the pDOS (partial density of states) for individual Pt atoms, which is the same for all core-shell nanoparticles (see Fig. S6 in Online Supplementary material). The core composition greatly influences the electronic properties of Pt atoms on the surface. To study this effect in more detail, we calculate the pDOS for each Pt atom on a nanoparticle surface with different core compositions and sizes.

The distribution of the  $d$ -band centers of surface Pt atoms depending on the compositions of the core for 1 nm (79 atoms) TM@Pt and HEA@Pt nanoparticles is shown in Fig. 3a. It is clear to see that amorphous nanoparticles have wider distribution of  $d$ -band center compared to fcc nanoparticles (red and blue, respectively, in Fig. 3a). This is associated with surface disorder, where all sites on the surface are symmetrically inequivalent caused by different chemical ordering compared to fcc structure. Width of distribution of  $d$ -band centers of surface atoms for fcc and amorphous 1 nm core-shell nanoparticles are shown in Fig. S7 (see Online Supplementary material). Considering nanoparticles with fcc structure (red color in Fig. 3a), one can see distinct peaks of the  $d$ -band center of surface atoms. This is due to the fact that the structure is symmetrical and ordered with the only a few types of symmetrically inequivalent sites on the surface according to the nearest neighbors analysis.

The spatial distribution of  $d$ -band centers across the surface of nanoparticles is shown in Fig. 4b,f. Visually, it is clearly seen that the highest values are associated with Ag and Au cores. However, considering the distribution of  $d$ -band centers in amorphous nanoparticles (Fig. 4f), one can indicate a smooth change in the value of  $d$ -bands moving from the surface to the core, in contrast to fcc ones (Fig. 4b).

Analysis of the  $d$ -band center distribution for core-shell nanoparticles indicates that  $d$ -band center of surface Pt atoms in shell can be shifted by changing the composition of the core. For Cu, Ir, Rh, and Ru cores  $d$ -band center of the Pt atoms in the shell decreases, while in the case of Ag, Au, and Pd cores  $d$ -band center increases.

The case of the HEA core needs to be considered separately. Considering the  $d$ -band center of HEA@Pt nanoparticles, the distribution of  $d$ -band centers for surface Pt atoms in fcc and amorphous structures is almost identical. In contrast, for TM@Pt a very different distribution pattern is observed between fcc and amorphous materials. This is due to the fact that different atoms in HEA shift the  $d$ -band center of Pt atoms on the surface differently, forming a multitude of inequivalent adsorption sites.

The analysis of the  $d$ -band center distribution for larger core-shell nanoparticles (201 and 321 atoms) indicates that  $d$ -band center can

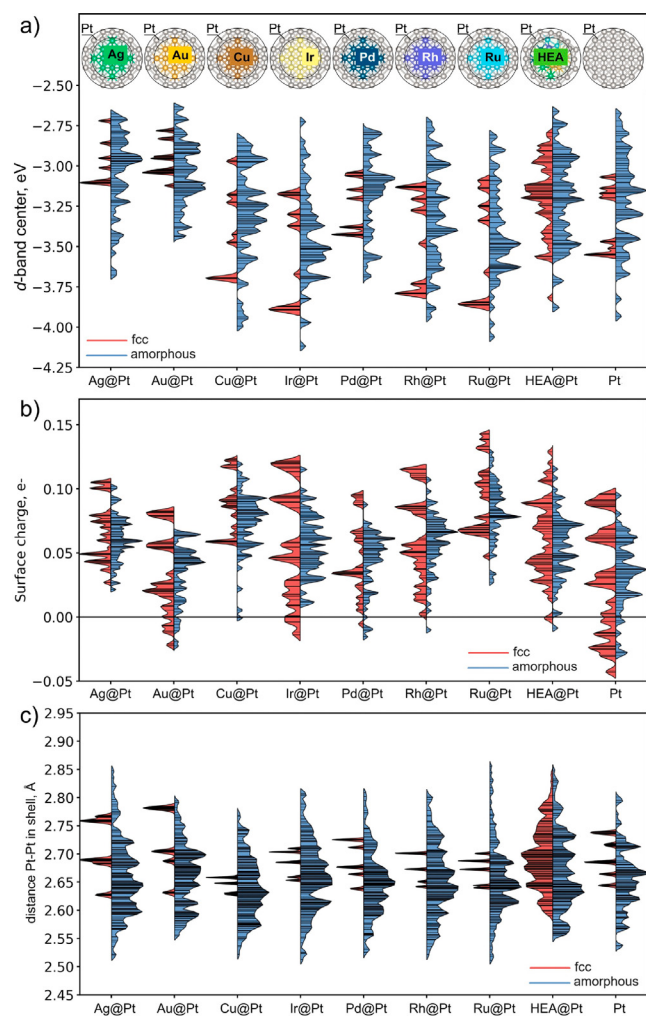


**Fig. 3.** Violin plots of distributions of (a) surface  $d$ -band centers, (b) surface charges, and (c) Pt-Pt distances between surface atoms on the composition of the core for 1 nm nanoparticles (79 atoms). The data for fcc structures are shown in red, and the data for amorphous structures are shown in blue.

be shifted by changing the core-to-shell ratio (Fig. S8 and Fig. S9 in Online Supplementary material). In the case of Au and Ag cores, we observe an upward shift of the  $d$ -band center of the surface Pt atoms as the core size increases and the shell size decreases. But in the case of Cu, Ir, Rh and Ru, we observe a slight shift down of the  $d$ -band center during an increase in the core size, while the shell size simultaneously decreases. In the case of 1.5 nm fcc nanoparticles with HEA core (Fig. 5a), increasing the core size while decreasing the shell size leads to an increase in the whole width of the  $d$ -band center distribution. In the case both fcc and amorphous HEA<sub>79</sub>@Pt<sub>122</sub> the distribution of the  $d$ -band center becomes practically the same, see Fig. S7 in the Online Supplementary material. Thus, by changing the composition and size of the core, it is possible to adjust the electronic properties of the surface atoms of Pt core-shell nanoparticles and this should lead to changes in their adsorption properties [114].

### 3.3. Charge

One of the main factors influencing the adsorption of different chemical agents on the surface is the uncompensated surface charge coming from the presence of broken bonds on the nanoparticle surface. Bader charge analysis [107] is used to investigate the surface charge

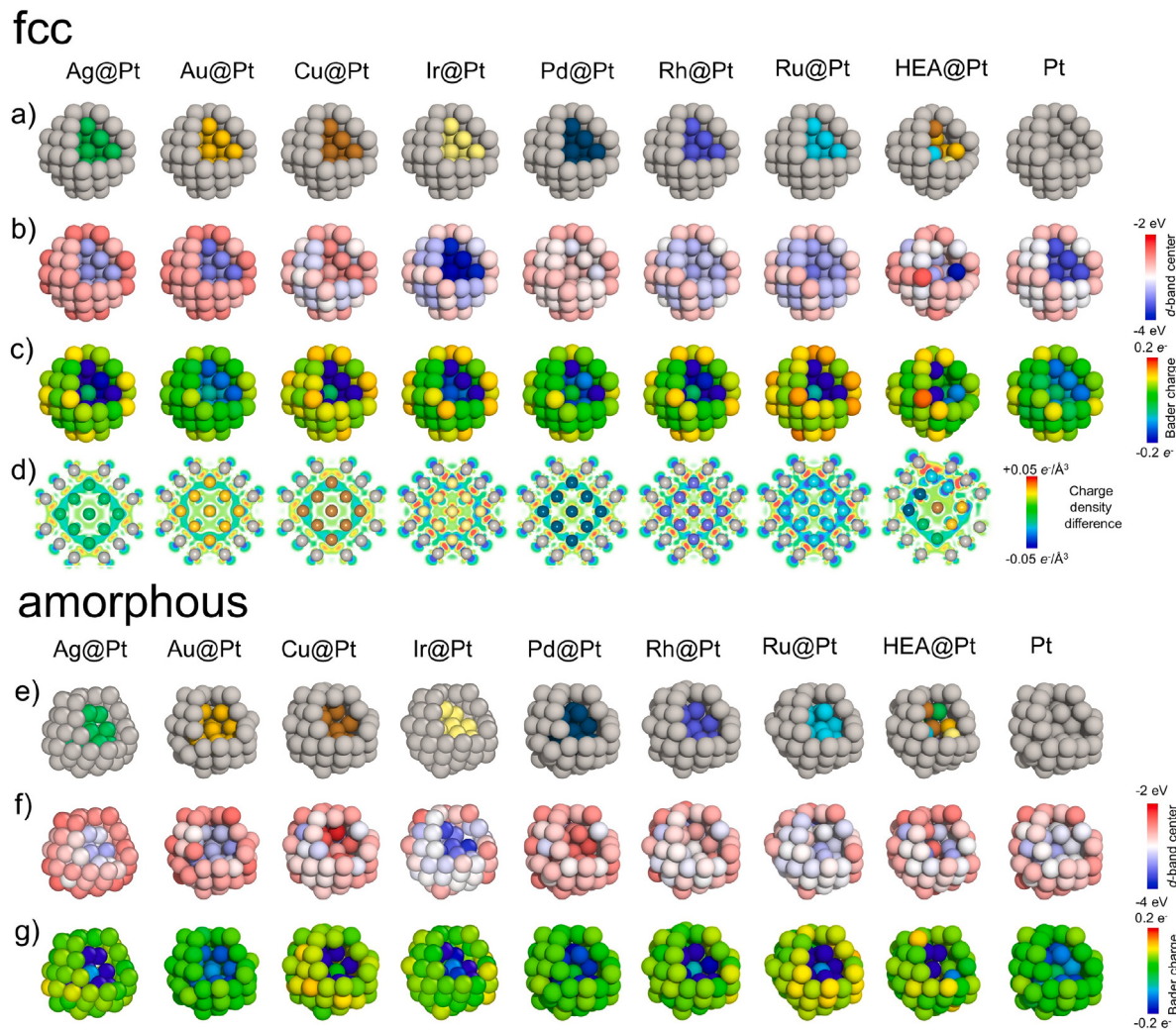


**Fig. 4.** Atomic structure of considered (a) fcc and (e) amorphous 1 nm (79 atoms) TM/HEA@Pt nanoparticles. Spatial distribution of (b,f) d-band centers, (c,g) charges for fcc and amorphous nanoparticles. (d) Charge density difference for fcc nanoparticles.

distribution of TM@Pt and HEA@Pt core–shell nanoparticles. The distributions of atomic charges on the surface of Pt atoms with different core compositions are shown in Fig. 3b for 1 nm nanoparticles (201 atoms). Comprehensive analysis of the electronic charge distribution revealed a consistent accumulation of excess negative charge localized on their surfaces. This phenomenon is observed universally across all nanoparticle systems investigated. Critically, the chemical composition of the nanoparticle core is found to exert a significant influence on the magnitude of this negative charge density on the surface Pt atoms. Our results demonstrate a clear correlation between the work function of metal in the core and the resulting surface charge on Pt. Cores composed of metals with lower work functions, such as Ag and Cu, induce a significantly more pronounced negative charge on platinum atoms than cores composed of higher-work-function metals. This effect is attributed to the enhanced electron transfer from the low work function core material to the Pt shell, driven by the difference in the Fermi levels upon contact. Consequently, the electronic structure and resulting chemical reactivity, especially catalytic properties, of the Pt surface can be evidently tuned through strategic selection of core metals based on intrinsic electronic parameters such as work function.

The relative sizes of the core and shell are an important factor governing charge redistribution on the nanoparticle surface. Our analysis reveals that modifications to the core–shell size ratio induce the most significant electronic perturbations in systems where the core consists of metals with the lowest work function, specifically Ag, Cu and Ru.

This can be seen from the data for 1.5 and 2 nm size nanoparticles with different core–shell size ratio in the Figures S10 and S11 in the Online Supplementary material. Remarkably, the condition of a monoatomic Pt layer encapsulating the core drives the most pronounced electron transfer phenomena. In this configuration, cores of Ag, Cu, or Ru facilitate the maximum achievable redistribution of electron density toward the Pt atoms within the shell (Figure S12 in the Online Supplementary material for 1.5 and 2 nm size nanoparticles with different core–shell size ratio). This effect is attributed to the synergistic interaction between the intrinsic low work function of the core metal and increased interfacial strain, together with quantum confinement effects inherent in the monolayer platinum shell. The resulting significant enrichment of the electron density on Pt atoms under ultra-thin Pt shells with low work function cores strongly suggests a powerful strategy for precisely tailoring electronic structures and, consequently, adsorption properties and catalytic activities in Pt-based nanocatalysts.

Our investigation of the core–shell size ratio effect in HEA@Pt nanoparticles revealed a significant enrichment of electrons on the surface of Pt atoms when the thickness of the Pt shell decreased while the size of the HEA core increased (Fig. 5b). This enhanced surface electron density in HEA@Pt nanoparticles of 1.5 nm size is directly visualized through the charge redistribution analysis in Fig. 6c,d,g. For TM@Pt charge redistribution refer to Fig. S13 in the Online Supplementary material. These data clearly demonstrate a distinct shift in the localization of electron density. Electrons transfer from HEA core

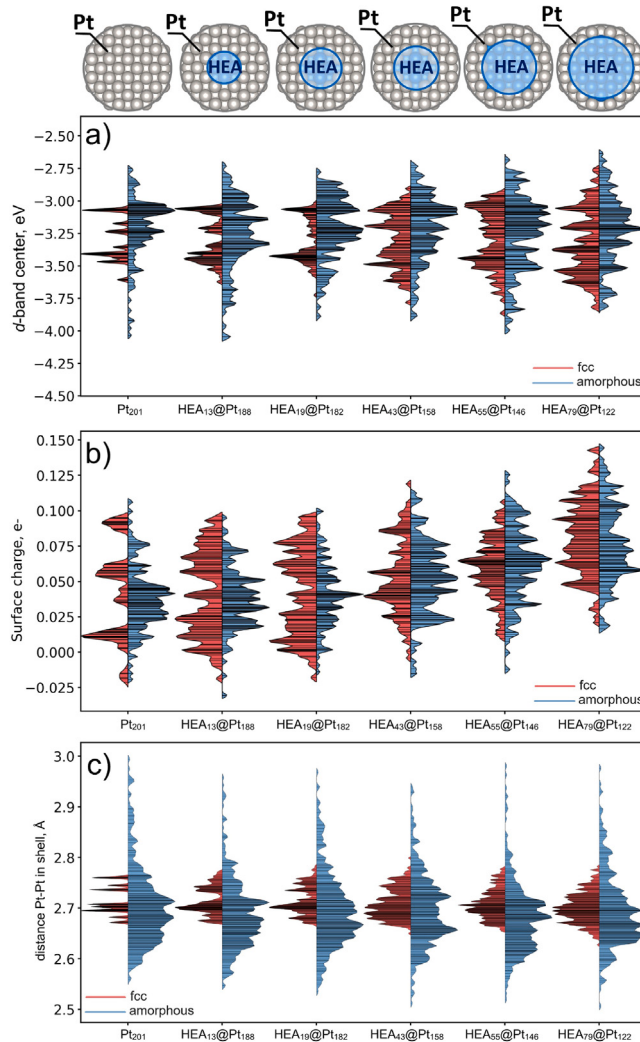


**Fig. 5.** Violin plots of distributions of (a) surface *d*-band centers, (b) surface charges, and (c) Pt-Pt distances between surface atoms depending on the size of the HEA core for 1.5 nm nanoparticles. The data for fcc structures are shown in red, and the data for amorphous structures are shown in blue.

atoms to the region proximal to the Pt shell, making it thinner and the core expanding. The trends in the surface charge change depend on the composition of the core and the core–shell size ratio, but there are some differences between fcc and amorphous structures. For fcc, there is a more pronounced and distinctive peak in surface charge compared to amorphous.

The observed charge redistribution is critically relevant for catalytic applications, where optimal adsorption of reactant molecules is governed by specific surface electronic properties [115,116]. Different molecules exhibit distinct charge preferences for favorable binding. For example CO adsorption preferentially occurs at positively charged sites. This preference arises because CO usually acts as a sigma-donor, and its binding is strengthened by the ability to donate electrons to vacant orbitals on a surface site that is less negatively charged (or more positively charged) [117–119]. Conversely, the O<sub>2</sub> molecule acts as an electron acceptor, relying on back-donation into its antibonding  $\pi^*$  orbitals. Consequently, O<sub>2</sub> exhibits stronger interaction with and preferential adsorption on negatively charged surface sites [120]. Therefore, the ability to precisely tune surface charge redistribution through structural engineering – manipulating core composition, core–shell size ratio, and crystallinity (fcc vs. amorphous) – provides a powerful strategy for tailoring nanoparticle surface properties. This control opens

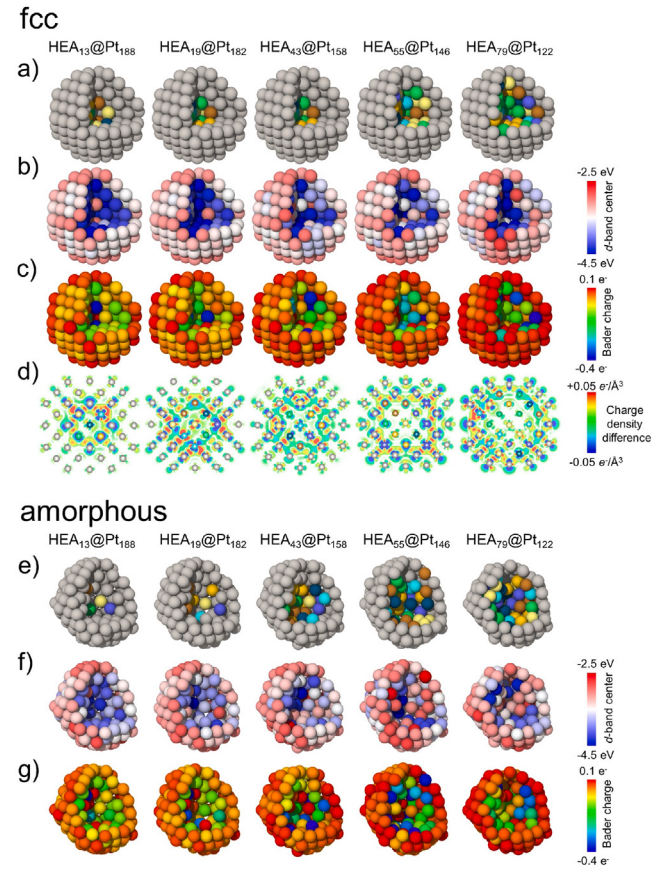


**Fig. 6.** Atomic structure of considered (a) fcc and (e) amorphous 1.5 nm (201 atoms) HEA@Pt nanoparticles. Spatial distribution of (b,f) *d*-band centers, (c,g) charges for fcc and amorphous nanoparticles. (d) Charge density difference for fcc nanoparticles.

up new ways for designing highly selective and active catalysts for a variety of reactions. This phenomenon of structure/composition-dependent charge redistribution in TM@Pt and HEA@Pt core–shell nanoparticles aligns with detailed observations in our prior studies on PtPd, CuAu, IrPd and PdAu core–shell nanoparticles [25–28,121].

#### 3.4. Strain effect

The modulation of surface charge and *d*-band center position in core–shell nanoparticles governed by core composition can be also attributed to core-induced lattice strain in the Pt shell, as established theoretically and experimentally [29]. This mechanistic link arises because the equilibrium lattice parameter of the shell adapts to the crystallographic constraints imposed by the core, directly perturbing the electronic structure. A compelling illustration comes from Guan et al. [122] where they performed a DFT study on a Pt monolayer deposited on Au(111). Their calculations revealed that the Au substrate expands the Pt monolayer lattice by 4.3% (from 2.77 to 2.89 Å). This tensile strain, combined with Pt-Au orbital hybridization, shifts the *d*-band center by 0.69 eV toward the Fermi level. Such *d*-band shift enhances surface reactivity by strengthening adsorbate binding via enhanced back-donation. Similar strain effects were observed in other systems, for example Zhang et al. [123] demonstrated core-dependent interatomic distance variations in Au@Pd nanoparticles, confirming the universality of this phenomenon. In our work, we quantitatively correlate core composition with surface lattice expansion/contraction Pt across diverse nanoparticle architectures.

**Fig. 3c** shows how the Pt shell adjusts its interatomic spacing to minimize the mismatch between the core and shell lattice constants. This is achieved by compressive strain on cores with smaller lattice parameters, such as Cu (3.61 Å), and tensile strain on cores with larger lattice parameters, like Au (4.08 Å) or Ag (4.09 Å). Crucially, this core-induced strain is significantly attenuated in amorphous structures despite identical compositions. Core–shell size ratio variations maximize Pt–Pt bond alterations when lattice mismatch exceeds 4% (Fig. S14 in the Online Supplementary material), particularly for Ag/Cu/Au cores. Strikingly, HEA@Pt nanoparticles exhibit very similar distribution of Pt–Pt distances in both fcc and amorphous structures, see **Fig. 3c**. This suggests that multi-component core leads to the same effect of local strain fields redistribution as amorphization. In experimental synthesis, such strain redistribution may enhance structural stability and reduce the likelihood of defect formation or shell delamination.

The distinct advantage of a multi-component HEA core over a single-TM core lies in its synergistic and structural effects on the properties of the Pt shell, including strain redistribution and electronic indistinguishability of atoms. While single-TM cores impose uniform, and often extreme strain and electronic perturbations such as the strong compression from Cu or tensile strain from Ag, a HEA core averages these competing influences. This results in a smooth redistribution of the mechanical strain field, mitigating local extremes, and a collective electron transfer, enriching the Pt surface charge beyond a simple linear average of its constituents. Consequently, the HEA core generates a spectrum of active sites on the Pt surface where each atom is tuned by a unique local chemical environment beneath it.

These findings establish lattice strain engineering as a dual strategy alongside charge redistribution to tune catalytic surfaces. By controlling core composition and size ratios, we precisely manipulate both geometric (strain) and electronic (*d*-band, charge) descriptors to optimize activity and selectivity.

### 3.5. Adsorption properties

In order to determine the influence of structure and core composition on the adsorption energy, we calculate the adsorption energies of CO, NO, CH<sub>3</sub>, and NH<sub>3</sub> on each inequivalent site on the surface of TM@Pt and HEA@Pt nanoparticles with a diameter of 1 nm (79 atoms). In total 60 adsorption **top** sites and ~120 **hollow** sites are calculated for each TM@Pt and HEA@Pt nanoparticle for each molecule (i.e. CO, NO, CH<sub>3</sub>, and NH<sub>3</sub>). The distributions of adsorption energies for CO, NO, CH<sub>3</sub>, and NH<sub>3</sub> are shown in **Fig. 7**. The distributions of the adsorption energy depending on the site (**top** or **hollow**) for all nanoparticles and molecules are shown in Fig. S15–18 in the Online Supplementary material.

First of all, we compare the adsorption energies obtained for Pt<sub>79</sub> with an fcc structure to the results of previous work. Our calculated CO adsorption energies on Pt<sub>79</sub> nanoparticles exhibit excellent agreement with reported slab values for Pt(111) from Carbone et al. [124]. Their work found adsorption energies of -1.82 eV for the top site and -1.94 eV for the hollow site. Our corresponding results for the (111) facet of the Pt<sub>79</sub> nanoparticle are -1.92 eV (top) and -2.00 eV (hollow). Nanba et al. [125] have showed that the adsorption energy of NO on the surface of a Pt<sub>405</sub> nanoparticle varies from -1.5 to 2.3 eV depending on the adsorption site. This is consistent with our results for a Pt<sub>79</sub> where the adsorption energy varies from -1.6 to -2.3 eV depending on the site.

Analyzing the influence of nanoparticle structure on adsorption energy distribution for selected molecules, one can clearly see that in the fcc case, the distribution has several distinct peaks depending on the adsorption site, see **Fig. 7**. The adsorption energy distributions for amorphous nanoparticles are quite different. The distribution is smeared due to the presence of many non-equivalent adsorption sites on the surface compared to fcc nanoparticles. For HEA@Pt core–shell

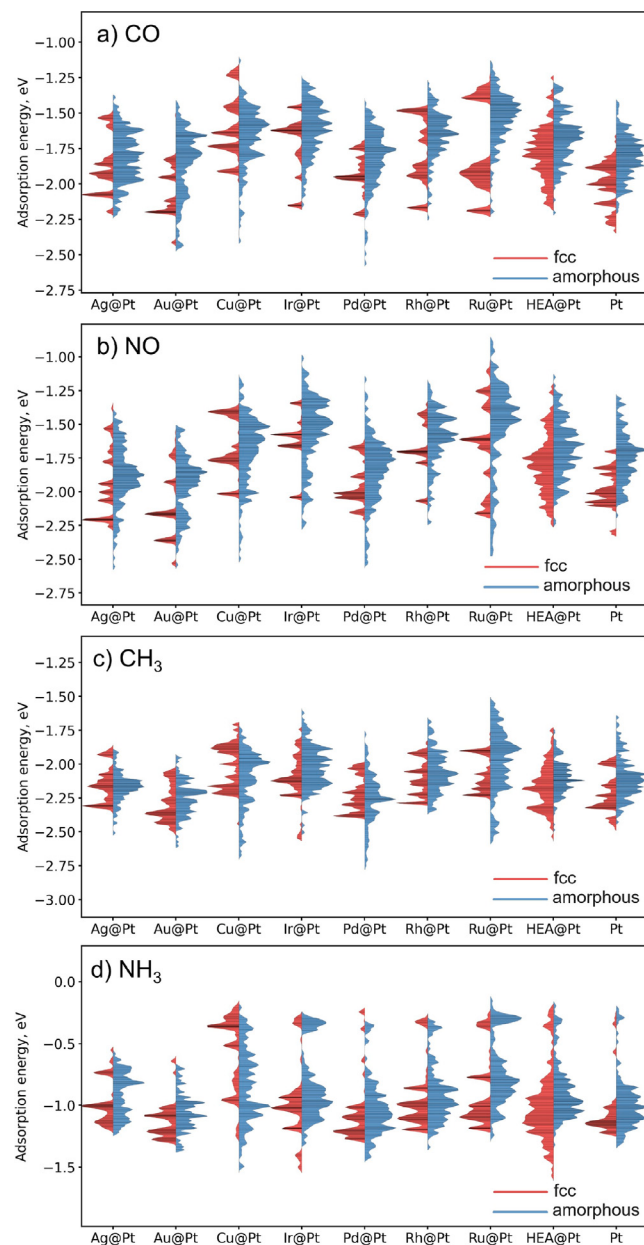


**Fig. 7.** The violin plot showing the distribution of adsorption energies of (a) CO, (b) NO, (c) CH<sub>3</sub> and (d) NH<sub>3</sub> on TM@Pt and HEA@Pt nanoparticles (1 nm, 79 atoms) with fcc and amorphous structures.

nanoparticles, the adsorption energy distributions exhibit a remarkable similarity between the fcc-crystalline and amorphous structures. This similarity is attributed to the dominant electronic and geometric modifications induced by HEA in the core, see **Fig. 7**.

Analyzing the change in adsorption energy distribution depending on core composition, one can clearly see how adsorption energies of various molecules vary greatly depending on transition metal in the core. In particular, in the case of NH<sub>3</sub> adsorption on Ag@Pt and Cu@Pt the difference can be almost twice (**Fig. 7d**). Also, adsorption energy is highly dependent on core composition for TM@Pt nanoparticles with CO and NO (**Fig. 7a,b**) and the effect of core composition on CH<sub>3</sub> is not as pronounced (**Fig. 7c**).

The width of the adsorption energy distribution is a fundamental descriptor that governs both the rate and selectivity of catalytic reactions by providing a spectrum of active sites for different elementary steps.

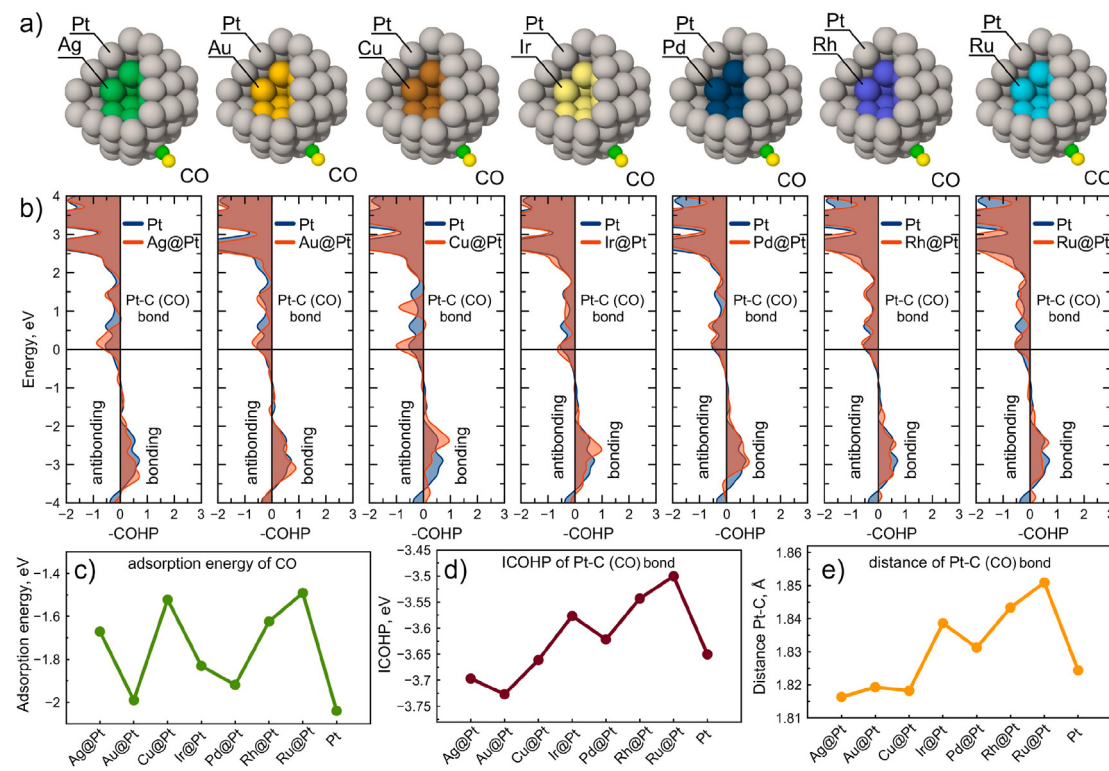


**Fig. 8.** (a) Atomic structures of TM@Pt nanoparticles with adsorbed CO molecules. (b) Calculated COHP diagrams for Pt-C bonding. (c) Dependence of CO adsorption energy on core composition in TM@Pt nanoparticles. (d) Dependence of ICOHP on core composition in TM@Pt nanoparticles. (e) Dependence of Pt-adsorbate distance on core composition in TM@Pt nanoparticles.

This principle was elegantly demonstrated by Chen et al. [126] in their study of the hydrogen evolution reaction, where they revealed that the activity of a Pt/C<sub>60</sub> catalyst is directly linked to the diversity of its binding sites, as quantified by the distribution widths for the adsorption of H, OH, and H<sub>2</sub>O. Their computational results establish that a spectrum of adsorption strengths, rather than a single optimal value, is a crucial factor for achieving higher catalytic performance. This concept extends directly to complex alloy systems, as shown by Huang et al. [82] in a comparative study of disordered and crystallized PtRhPdIrRu HEA NPs. They attributed a significant enhancement in HER activity to structural disorder, demonstrating that disordered nanostructures host a high density of non-equivalent adsorption centers. This structural characteristic generates a broad distribution of adsorption energies for intermediates like H and OH, which is pivotal for optimizing performance.

Importantly, a detailed computational study by Chepkasov et al. [26] provides a direct atomic-level comparison of how non-equilibrium structures dictate these adsorption properties. In their work simulating the gas-phase synthesis of Cu-Au nanoparticles, they found that the resulting amorphous, icosahedral, and fcc structures exhibit profoundly different adsorption site diversities. Density functional theory calculations revealed that amorphous Cu-Au clusters expose a wider variety of non-equivalent sites for CO and O adsorption compared to their fcc counterparts. For instance, while the fcc cluster featured strongly-binding Cu<sub>3</sub> sites for O, the amorphous cluster uniquely stabilized O on mixed Au<sub>1</sub>Cu<sub>2</sub> sites and provided a broader range of CO binding energies. This heterogeneity in site geometry and composition directly translates to a broader adsorption energy distribution on the amorphous nanoparticles. Consequently, the Brønsted–Evans–Polanyi (BEP) relations for CO oxidation were markedly different for the amorphous clusters, showing low sensitivity of the activation energy to the reaction energy across its diverse sites. In contrast, the fcc and icosahedral clusters followed a steeper BEP relation where the activity was highly sensitive to the local O binding strength. This work by Chepkasov

et al. [26] conclusively demonstrates that the non-equilibrium, disordered structure of amorphous nanoparticles inherently provides a wider adsorption energy distribution, which can lead to distinct and potentially superior catalytic performance by enabling a more versatile interaction with multiple reaction intermediates.

To comprehensively investigate the influence of core composition on Pt-C chemical bonding in CO and CH<sub>3</sub> adsorption systems, we conducted Crystal Orbital Hamilton Population (COHP) analyses, with the resulting -COHP diagrams (Fig. 8b, and Fig. 9b red traces) systematically compared against pure Pt references (blue traces). All core–shell configurations exhibit pronounced antibonding states near the Fermi level, with transition metal cores such as Cu significantly intensifying these antibonding characteristics in CO adsorption scenarios, thereby directly destabilizing the Pt-C bonding interaction. Quantitative analysis integrating adsorption energies (ICOHP, where more negative values indicate stronger bonds) and Pt-adsorbate distances (Fig. 8c,d,e and Fig. 9c,d,e) demonstrates that the core composition profoundly modulates bond strength and molecular adsorption geometry. These alterations arise from core-driven electron density redistribution at Pt-adsorbate interfaces, directly perturbing chemical bonding landscapes. The core with low work function (Cu, Ru, Ag) donates excess electrons to the Pt shell, populating antibonding orbitals in the Pt-C system. Simultaneously, lattice mismatch-induced strain (notably compressive strain from the Cu-core's 7.9% lattice contraction relative to Pt) geometrically distorts the bonding orbitals. For CH<sub>3</sub> adsorption, the core sensitivity is attenuated due to its dominant σ-donor character, though antibonding features persist. Collectively, this electronic restructuring fundamentally reconfigures the chemical bonding landscape at catalytic interfaces, demonstrating how core engineering directly modulates adsorbate bond strength through intertwined electronic and strain effects.

We also explored the impact of altering the sizes of the core and shell within core–shell nanoparticles on the subsequent variation in adsorption energy. The adsorption of CO, NO, CH<sub>3</sub>, and NH<sub>3</sub> at the

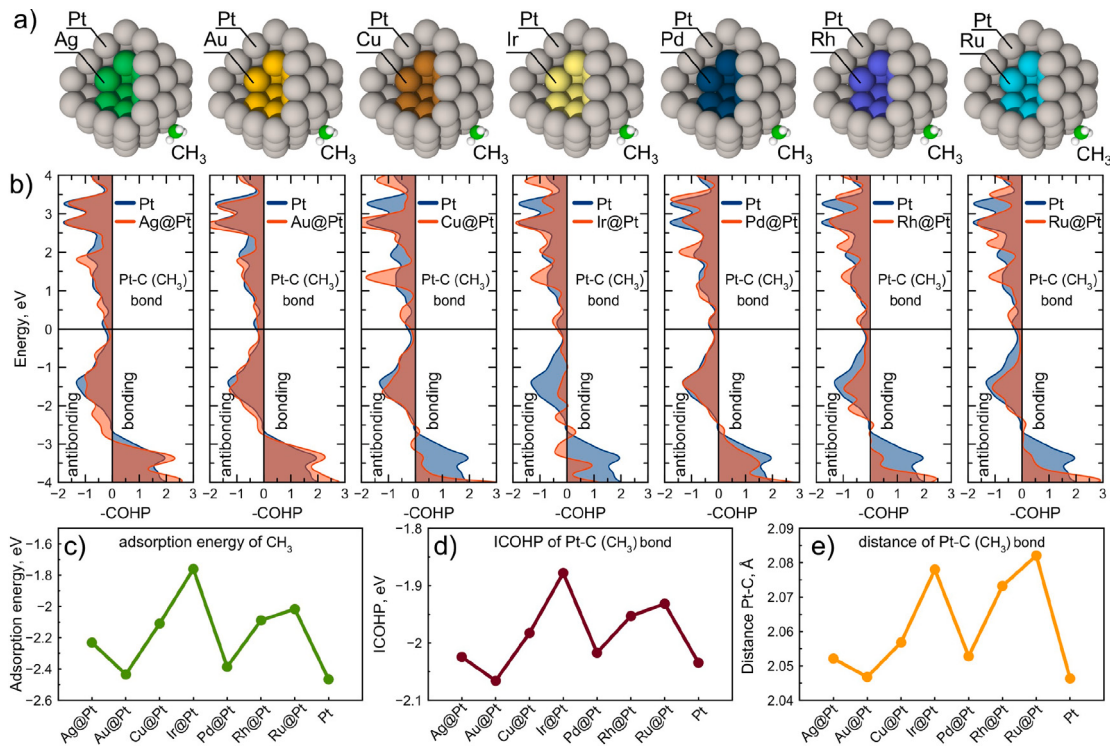


**Fig. 9.** (a) Atomic structures of TM@Pt nanoparticles with adsorbed CH<sub>3</sub> molecules. (b) Calculated COHP diagrams for Pt-C bonding. (c) Dependence of CH<sub>3</sub> adsorption energy on core composition in TM@Pt nanoparticles. (d) Dependence of ICOHP on core composition in TM@Pt nanoparticles. (e) Dependence of Pt-adsorbate distance on core composition in TM@Pt nanoparticles.

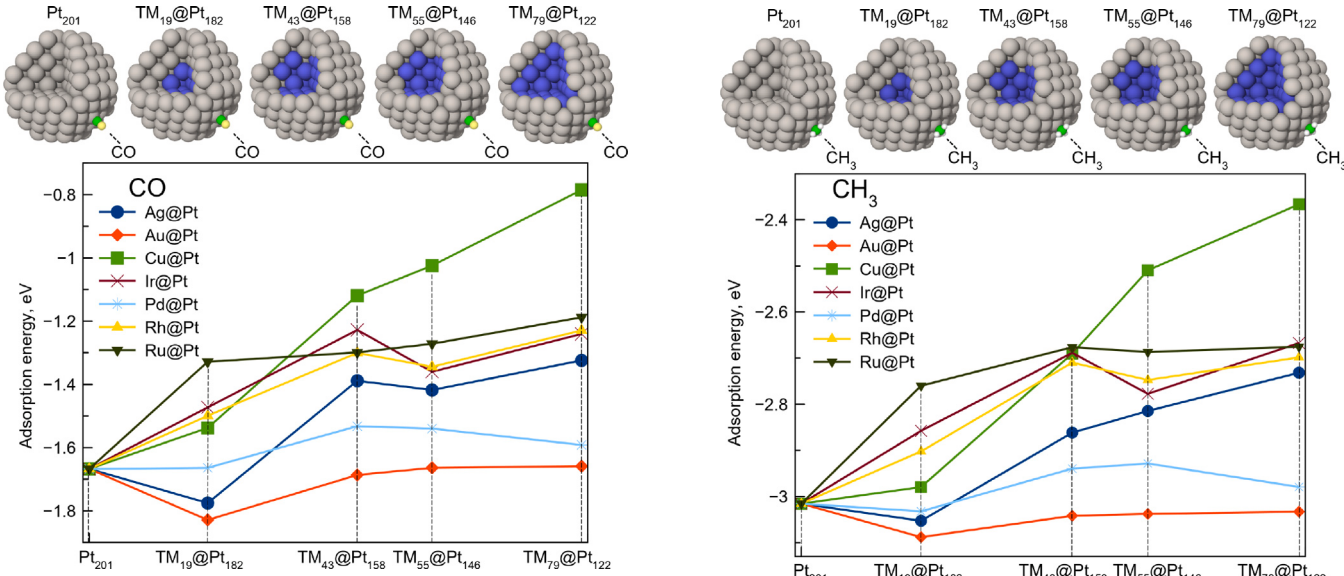


**Fig. 10.** Dependence of the adsorption energy of CO on the top site of the 1.5 nm TM@Pt nanoparticles (201 atoms, (111) facet) on core–shell size ratio. The CO molecule is located at the same site for nanoparticles with different core sizes.

same adsorption site (top position) on a (111) facet of nanoparticle with a diameter of 1.5 nm (201 atoms) is considered. Nanoparticles with 19, 43, 55, 79 atoms in the TM core, and 188, 182, 158, 146, and 122 Pt atoms in the shell are considered. Pure Pt nanoparticle is also calculated for comparison. The dependencies of the adsorption energy on the core–shell size ratio are shown in Figs. 10 and 11 for CO and CH<sub>3</sub>. Adsorption energy distribution for the cases of NO and NH<sub>3</sub> are shown

in Fig. S19 and S20 in the Online Supplementary material. It is evident that even the smallest core (19 atoms) already changes the adsorption properties of the platinum shell of a nanoparticle. This long-range effect of the core on surface properties is consistent with the previous results obtained by Liu et al. [43], who systematically investigated the effect of thickness of Pt layer on activity of ORR catalysts. The Cu core changes

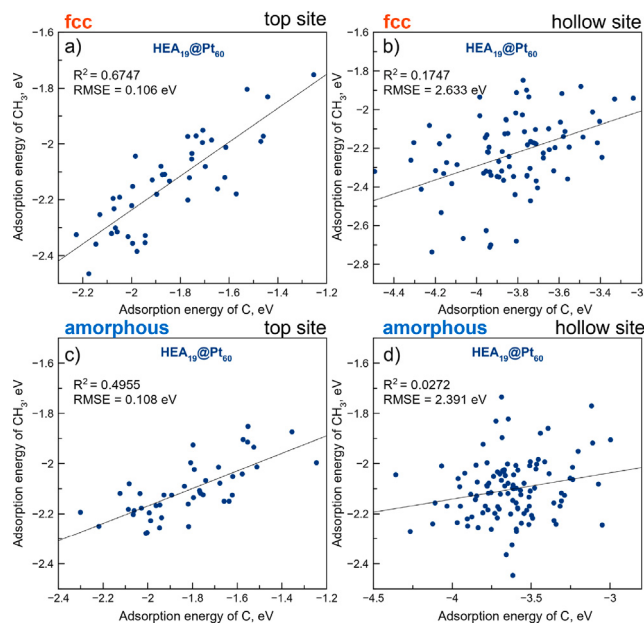


**Fig. 12.** The correlation between adsorption energy of CH<sub>3</sub> and C in the same sites on HEA<sub>19</sub>@Pt<sub>60</sub> nanoparticle with fcc and amorphous structure.

the adsorption properties of Pt the most strongly, apparently due to a strong mismatch (7.9%) in the lattice parameters of Cu (3.61 Å) and Pt (3.92 Å), and the Cu core strongly compresses the Pt shell, changing its adsorption properties.

Consequently, targeted manipulation of core size and composition (controlling strain/charge) and nanoparticle crystallinity (fcc vs. amorphous) provides deterministic control over Pt shell adsorption landscapes. Fcc structure localizes adsorption energies into discrete regions through site-specific electronic environments, while amorphous structures generate broad quasi-continuous energy distributions via surface heterogeneity. This dual-parameter control facilitates reaction-specific optimization of catalytic interfaces.

Building on the distinct adsorption behaviors observed in HEA<sub>n</sub>@Pt nanoparticles, we further propose that the inverse configuration where a monometallic core is coated with a high-entropy alloy shell (M@HEA) represents a promising alternative strategy for designing advanced catalytic surfaces. In such systems, the inherently heterogeneous and complex HEA shell itself can provide a diversity of active sites, enabling fine-tuning of adsorption properties [127,128]. This concept is supported by recent synthetic advances, for instance, Liu et al. [129] successfully designed Pd@PdPtRhIrRu core–shell nanocrystals through precise control of precursor reduction kinetics. Their work demonstrates that by carefully engineering the surface composition, shell-HEA nanostructures can achieve superior catalytic performance and enhanced durability, making them highly promising candidates for a wide range of advanced catalytic applications.

### 3.6. Adsorption energy vs. descriptors correlation

Previously, Nørskov et al. showed a good scaling relationship between a single atomic adsorbate and its hydrides with the same bond geometry, e.g., O vs. OH, C vs. CH<sub>n</sub>, and N vs. NH<sub>n</sub> [130,131]. However, their relationships were based on data obtained from metal surfaces, which only have a few possible adsorption sites. In contrast, nanoparticles have a much more complex situation related to composition and structure, as discussed above. Therefore, in this work we decided to test an approach to estimating the adsorption energy of CH<sub>n</sub> molecules based only on the adsorption energy of the C atom.

Considering the correlation between CH<sub>3</sub> and C, we calculate the adsorption energy of a C atom at each inequivalent site on the surface

of TM@Pt and HEA@Pt nanoparticles (1 nm, 79 atoms). It has 60 different adsorption sites for C atoms at the top sites and ~120 hollow sites per each TM@Pt and HEA@Pt nanoparticle like in the case of CH<sub>3</sub>. The distributions of adsorption energies of C atom are shown in Fig. S21 in the Online Supplementary material. The distribution of adsorption energy of C atom depending on the site (top or hollow) for all nanoparticles is shown in Fig. S22 in the Online Supplementary material. Similar to the cases of adsorption of CO, NO, CH<sub>3</sub> and NH<sub>3</sub> molecules, the adsorption energy for a C atom changes depending on the core composition. Different distribution patterns are observed for fcc and amorphous structures. However, comparing different adsorption sites, it is clear that the difference between the top and hollow sites is almost twice (~ 2 eV for the top site and ~ 4 eV for a hollow site). The lower adsorption energy of a C atom at a hollow adsorption site may be due to the fact that a C atom in this adsorption site is bounded to 3 Pt atoms, which increases its adsorption energy.

To evaluate the correlation between the adsorption energy of CH<sub>3</sub> and C observed by Nørskov et al. we use HEA<sub>19</sub>@Pt<sub>60</sub> nanoparticles with fcc and amorphous structures. This is done to understand how this descriptor works in the case of complex surfaces, such as the surfaces of nanoparticles. The correlations between the adsorption energies for CH<sub>3</sub> and C on HEA<sub>19</sub>@Pt<sub>60</sub> are shown in Fig. 12. As can be seen from the correlations in Fig. 12a, the best correlation between the adsorption energies of CH<sub>3</sub> and C is observed for the fcc structure at the top sites ( $R^2 = 0.67$ ), while the correlation for the amorphous structure is slightly worse ( $R^2 = 0.49$ ), due to electronic heterogeneity caused by topological disorder (see Fig. 12c). Critically, hollow sites do not display a meaningful correlation ( $R^2 = 0.17$  for fcc and  $R^2 = 0.02$  for amorphous) across both structures, see Fig. 12b,d. This is due to three-fold coordination, which induces multicenter bonding and redistributes charges asymmetrically. This introduces steric constraints and modifies orbital hybridization, disrupting the CH<sub>3</sub>/C simple scaling observed for directional  $\sigma$ -bonding at the top sites.

The correlations between the d-band center and surface charge of HEA<sub>19</sub>@Pt<sub>60</sub> nanoparticle with fcc and amorphous structures with adsorbed CO, NO, CH<sub>3</sub> and NH<sub>3</sub> molecules are also analyzed. The results of these correlations are presented in Fig. 13 for the d-band center and Fig. S20 for the charge. The d-band center exhibits fine correlations ( $R^2 = 0.43 - 0.46$ ) with the adsorption energies of CO, NO, and CH<sub>3</sub> at the top sites of fcc nanoparticles. This is consistent with the established d-band theory for  $\pi$ -backbonding and  $\sigma$ -donation adsorbates. These correlations significantly deteriorate for non-top sites and amorphous structures due to disrupted orbital hybridization and heterogeneous electronic environments. Notably, NH<sub>3</sub> adsorption shows no d-band correlation ( $R^2 < 0.1$ ) even at fcc top sites, reflecting its lone-pair donation mechanism. The correlation of adsorption energies with charge did not show any dependence in all the studied cases (see Fig. S23 in the Online Supplementary material). Thus, geometric disorder in amorphous structures and complex high-entropy alloys necessitates multi-descriptor models combining d-band center, charge transfer, and local coordination to predict adsorption energies. Advanced machine learning techniques, such as graph neural networks (GNNs), can be used to construct complex descriptors that takes into account local atomic environments, binding site heterogeneity etc. [132,133]. Interpretable machine learning methods, like symbolic regression, can distill complex adsorption descriptors into physically meaningful equations, bridging data-driven and theoretical approaches [134,135]. The application of machine learning methods to search for descriptors of multicomponent and high-entropy catalytic nanoparticles is currently a hot and important topic. This is evidenced by recent works on this topic [136–139] where several approaches were tested.

### 4. Conclusion

In conclusion, the study demonstrates that the catalytic performance of Pt-shell nanoparticles is critically dictated by the core composition

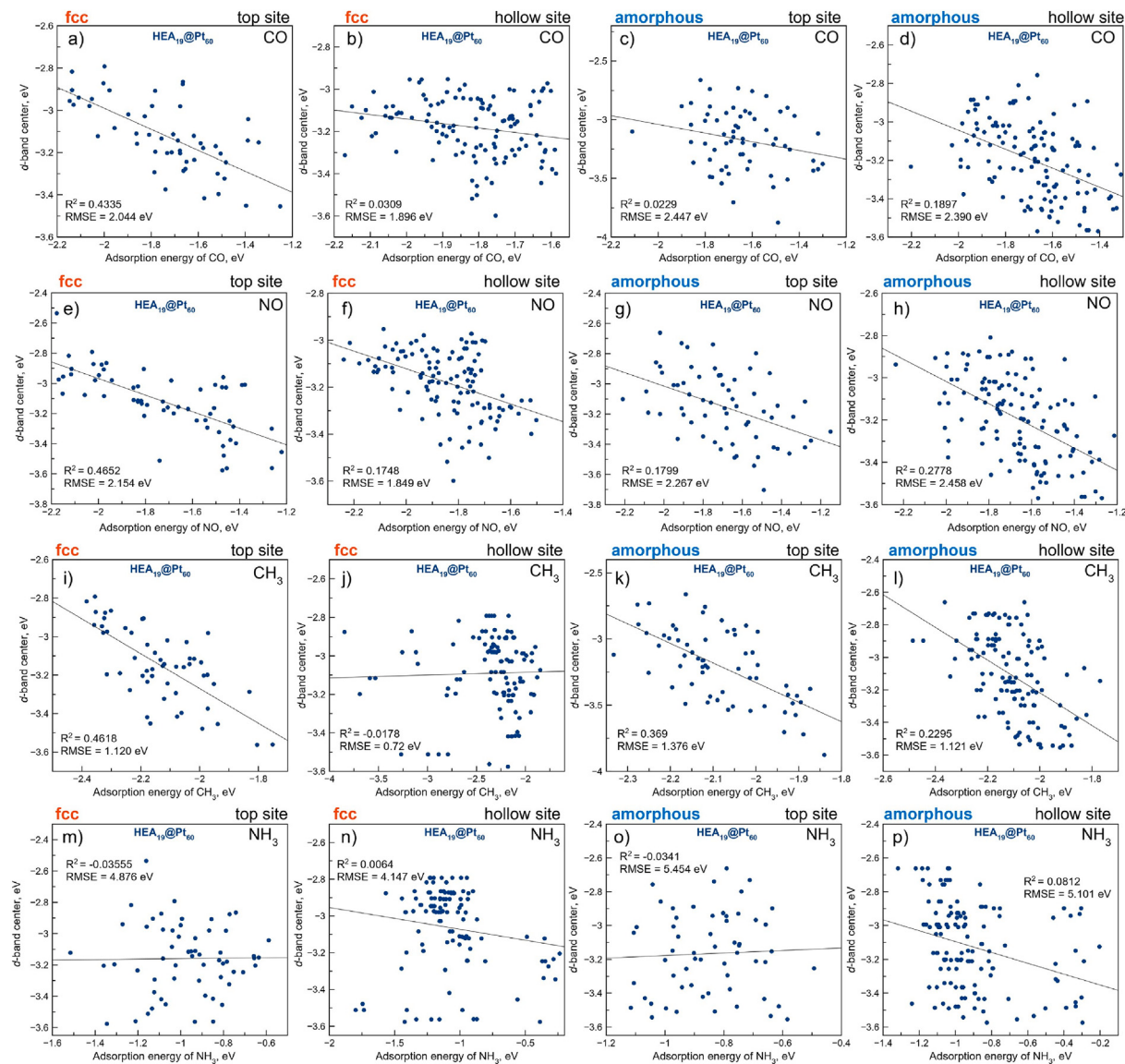


**Fig. 13.** The correlation between adsorption energy of CO, NO, CH<sub>3</sub> and NH<sub>3</sub> and d-band center on HEA<sub>19</sub>@Pt<sub>60</sub> nanoparticle with fcc and amorphous structure.

(transition metals or high-entropy alloys) and the structural state (cristalline fcc vs amorphous). Core-induced effects, including electronic charge redistribution, lattice strain, and shifts in the d-band center of surface Pt atoms collectively tune adsorption energies for key molecules (CO, NO, CH<sub>3</sub> and NH<sub>3</sub>). The low work function of core atoms (Ag, Cu, Ru) increases the electron density on the Pt surface, facilitating the adsorption of electron acceptors. At the same time, core atoms with high work functions strengthen the binding of electron donors such as CO. Strain effects driven by lattice mismatch between core and shell modulates the Pt-Pt distance and reactivity. The tensile strain (Au/Ag core) shifts the d-band center up, whereas compressive strain (Cu core) shifts it down. Amorphous structures exhibit broad quasi-continuous adsorption energy distributions due to heterogeneous surface sites, contrasting with discrete peaks in ordered fcc structures. The HEA cores uniquely redistribute strain and electronic effects in both structural states, creating multiple inequivalent active sites. Reducing the Pt shell thickness enhances charge transfer and strain, particularly for low work function cores, while the HEA core increases the surface electron density as the shell becomes thinner. Adsorption scaling relationships (e.g., CH<sub>3</sub> vs. C) hold for top sites in fcc structures but fail for hollow sites due to multisite bonding. These findings guide the rational design of Pt-shell catalysts and HEA cores and amorphous structures, which

enable superior tunability, stability, and reactivity while minimizing Pt usage and maximizing performance through synergistic control of geometric and electronic properties.

#### CRediT authorship contribution statement

**Ilya V. Chepkasov:** Writing – review & editing, Writing – original draft, Visualization, Methodology, Investigation, Formal analysis, Data curation, Conceptualization. **Viktor S. Baidyshev:** Software, Investigation. **Alexander G. Kvashnin:** Writing – review & editing, Visualization, Supervision.

#### Declaration of competing interest

The authors declare that they have no known competing financial interests or personal relationships that could have appeared to influence the work reported in this paper.

#### Acknowledgments

The research was carried out using resources of the Center for the Information and Computing of Novosibirsk State University and Zhores supercomputers at Skoltech.

## Appendix A. Supplementary data

Supplementary material related to this article can be found online at <https://doi.org/10.1016/j.mtener.2025.102130>.

## Data availability

Data will be made available on request.

## References

- [1] K. Sasaki, K.A. Kuttiiyiel, R.R. Adzic, Designing high performance pt monolayer core-shell electrocatalysts for fuel cells, *Curr. Opin. Electrochem.* 21 (2020) 368–375.
- [2] K.A. Kuttiiyiel, Y. Choi, S.-M. Hwang, G.-G. Park, T.-H. Yang, D. Su, K. Sasaki, P. Liu, R.R. Adzic, Enhancement of the oxygen reduction on nitride stabilized pt-M (M=Fe, Co, and Ni) core-shell nanoparticle electrocatalysts, *Nano Energy* 13 (2015) 442–449.
- [3] J. Shin, J.-H. Choi, P.-R. Cha, S.K. Kim, I. Kim, S.-C. Lee, D.S. Jeong, Catalytic activity for oxygen reduction reaction on platinum-based core-shell nanoparticles: all-electron density functional theory, *Nanoscale* 7 (38) (2015) 15830–15839.
- [4] S. Bai, C. Wang, M. Deng, M. Gong, Y. Bai, J. Jiang, Y. Xiong, Surface polarization matters: Enhancing the hydrogen-evolution reaction by shrinking Pt shells in Pt-Pd-graphene stack structures, *Angew. Chem. Int. Ed.* 53 (45) (2014) 12120–12124.
- [5] T. He, W. Wang, F. Shi, X. Yang, X. Li, J. Wu, Y. Yin, M. Jin, Mastering the surface strain of platinum catalysts for efficient electrocatalysis, *Nature* 598 (7879) (2021) 76–81.
- [6] A. De Clercq, O. Margeat, G. Sitja, C.R. Henry, S. Giorgio, Core-shell Pd-Pt nanocubes for the CO oxidation, *J. Catalysis* 336 (2016) 33–40.
- [7] A.K. Datye, M. Votsmeier, Opportunities and challenges in the development of advanced materials for emission control catalysts, *Nat. Mater.* 20 (8) (2021) 1049–1059.
- [8] X. Yang, F. Cheng, Z. Tao, J. Chen, Hydrolytic dehydrogenation of ammonia borane catalyzed by carbon supported Co core–Pt shell nanoparticles, *J. Power Sources* 196 (5) (2011) 2785–2789.
- [9] Y. Fan, A. Girard, M. Waals, C. Salzemann, A. Courty, Ag@ Pt core-shell nanoparticles for plasmonic catalysis, *ACS Appl. Nano Mater.* 6 (2) (2023) 1193–1202.
- [10] Y. Fan, C. Salzemann, B. Tremblay, A. Girard, A. Courty, Colloidal Ag@ Pt core-shell nanoparticles for the catalytic reduction of nitrophenol, *ACS Appl. Nano Mater.* 7 (6) (2024) 6130–6138.
- [11] Y. Yang, C. Tan, Y. Yang, L. Zhang, B.-W. Zhang, K.-H. Wu, S. Zhao, Pt3Co@ Pt core@ shell nanoparticles as efficient oxygen reduction electrocatalysts in direct methanol fuel cell, *ChemCatChem* 13 (6) (2021) 1587–1594.
- [12] K. Sasaki, H. Naohara, Y. Choi, Y. Cai, W.-F. Chen, P. Liu, R.R. Adzic, Highly stable Pt monolayer on PdAu nanoparticle electrocatalysts for the oxygen reduction reaction, *Nat. Commun.* 3 (1) (2012) 1115.
- [13] R.R. Adzic, J. Zhang, K. Sasaki, M.B. Vukmirovic, M. Shao, J. Wang, A.U. Nilekar, M. Mavrikakis, J. Valerio, F. Uribe, Platinum monolayer fuel cell electrocatalysts, *Top. Catal.* 46 (2007) 249–262.
- [14] R.R. Adzic, Platinum monolayer electrocatalysts: tunable activity, stability, and self-healing properties, *Electrocatalysis* 3 (2012) 163–169.
- [15] C. Wang, M. Chi, D. Li, D. Strmcnik, D. Van der Vliet, G. Wang, V. Komanicky, K.-C. Chang, A.P. Paulikas, D. Tripkovic, et al., Design and synthesis of bimetallic electrocatalyst with multilayered Pt-skin surfaces, *J. Am. Chem. Soc.* 133 (36) (2011) 14396–14403.
- [16] L. Zhang, R. Iyyamperumal, D.F. Yancey, R.M. Crooks, G. Henkelman, Design of Pt-shell nanoparticles with alloy cores for the oxygen reduction reaction, *ACS Nano* 7 (10) (2013) 9168–9172.
- [17] L. Zhang, G. Henkelman, Computational design of alloy-core@ shell metal nanoparticle catalysts, *ACS Catal.* 5 (2) (2015) 655–660.
- [18] Y. Ren, B. Li, C. Lv, Z. Zang, L. Li, Z. Lu, X. Yang, X. Zhang, X. Yu, Stabilizing platinum-based electrocatalysts for oxygen reduction reaction in acid media: A mini review, *Int. J. Hydrg. Energy* (2023).
- [19] Z. Zhong, Y. Tu, L. Zhang, J. Ke, C. Zhong, W. Tan, L. Wang, J. Zhang, H. Song, L. Du, et al., Surface strain effect on electrocatalytic hydrogen evolution reaction of Pt-based intermetallics, *ACS Catal.* 14 (2024) 2917–2923.
- [20] Z. Wang, Y. Liu, S. Chen, Y. Zheng, X. Fu, Y. Zhang, W. Wang, Strain engineering of Pt-based electrocatalysts for oxygen reaction reduction, *Front. Energy* (2024) 1–22.
- [21] J.P. Jonasse, M.P. Perich, S.J. Turner, J.E. van der Hoeven, Synthetic control over lattice strain in trimetallic AuCu-core Pt-shell nanoparticles, *Nanoscale* 17 (12) (2025) 7100–7113.
- [22] J.E. van der Hoeven, J. Jelic, L.A. Olthof, G. Totarella, R.J. van Dijk-Moes, J.-M. Krafft, C. Louis, F. Studt, A. van Blaaderen, P.E. de Jongh, Unlocking synergy in bimetallic catalysts by core-shell design, *Nat. Mater.* 20 (9) (2021) 1216–1220.
- [23] M. Luo, S. Guo, Strain-controlled electrocatalysis on multimetallic nanomaterials, *Nat. Rev. Mater.* 2 (11) (2017) 1–13.
- [24] A.K. Singh, Q. Xu, Synergistic catalysis over bimetallic alloy nanoparticles, *ChemCatChem* 5 (3) (2013) 652–676.
- [25] I. Chepkasov, M. Visotin, E. Kovaleva, A. Manakhov, V. Baidyshev, Z. Popov, Stability and electronic properties of PtPd nanoparticles via MD and DFT calculations, *J. Phys. Chem. C* 122 (31) (2018) 18070–18076.
- [26] I.V. Chepkasov, V.S. Baidyshev, A.A. Golubnichiy, I.S. Zamulin, A.G. Kvashnin, S.M. Kozlov, Cu–Au nanoparticles produced by the aggregation of gas-phase metal atoms for CO oxidation: Special issue: Emerging investigators, *Aggregate* 3 (6) (2022) e273.
- [27] I.V. Chepkasov, V.S. Baidyshev, A.G. Kvashnin, Structure-driven tuning of o and CO adsorption on AuCu nanoparticles: A density functional theory study, *Phys. Rev. B* 108 (20) (2023) 205414.
- [28] I.V. Chepkasov, I.S. Zamulin, V.S. Baidyshev, A.G. Kvashnin, Tuning the surface properties of AuPd nanoparticles for adsorption of O and CO, *Phys. Chem. Chem. Phys.* 25 (48) (2023) 33031–33037.
- [29] I.V. Chepkasov, A.D. Radina, A.G. Kvashnin, Structure-driven tuning of catalytic properties of core-shell nanostructures, *Nanoscale* (2024).
- [30] I. Chepkasov, V. Baidyshev, V. Tsura, Molecular dynamic simulation of melting copper-silicon nanoparticles, in: *Journal of Physics: Conference Series*, 1015, (3) IOP Publishing, 2018, 032023.
- [31] V. Baidyshev, I. Chepkasov, N. Artemova, Study of thermal stability of disordered alloy AgxCu1-x nanoparticles by molecular dynamic simulations, in: *Journal of Physics: Conference Series*, 1015, (3) IOP Publishing, 2018, 032021.
- [32] I. Chepkasov, V. Baidyshev, A. Baev, Structural properties of CuAu nanoparticles with different type, molecular dynamic simulations, in: *Journal of Physics: Conference Series*, 1015, (3) IOP Publishing, 2018, 032022.
- [33] X. Wang, S.-I. Choi, L.T. Roling, M. Luo, C. Ma, L. Zhang, M. Chi, J. Liu, Z. Xie, J.A. Herron, et al., Palladium–platinum core-shell icosahedra with substantially enhanced activity and durability towards oxygen reduction, *Nat. Commun.* 6 (1) (2015) 7594.
- [34] M.B. Gawande, A. Goswami, T. Asefa, H. Guo, A.V. Biradar, D.-L. Peng, R. Zboril, R.S. Varma, Core-shell nanoparticles: synthesis and applications in catalysis and electrocatalysis, *Chem. Soc. Rev.* 44 (21) (2015) 7540–7590.
- [35] P. Strasser, S. Koh, T. Anniyev, J. Greeley, K. More, C. Yu, Z. Liu, S. Kaya, D. Nordlund, H. Ogasawara, et al., Lattice-strain control of the activity in dealloyed core-shell fuel cell catalysts, *Nat. Chem.* 2 (6) (2010) 454–460.
- [36] J. Rodriguez, Physical and chemical properties of bimetallic surfaces, *Surf. Sci. Rep.* 24 (7–8) (1996) 223–287.
- [37] M. Mavrikakis, B. Hammer, J.K. Nørskov, Effect of strain on the reactivity of metal surfaces, *Phys. Rev. Lett.* 81 (13) (1998) 2819.
- [38] L.A. Kibler, A.M. El-Aziz, R. Hoyer, D.M. Kolb, Tuning reaction rates by lateral strain in a palladium monolayer, *Angew. Chem. Int. Ed.* 44 (14) (2005) 2080–2084.
- [39] X. Yang, Y. Wang, X. Tong, N. Yang, Strain engineering in electrocatalysts: fundamentals, progress, and perspectives, *Adv. Energy Mater.* 12 (5) (2022) 2102261.
- [40] X. Mao, Z. Qin, S. Ge, C. Rong, B. Zhang, F. Xuan, Strain engineering of electrocatalysts for hydrogen evolution reaction, *Mater. Horizons* 10 (2) (2023) 340–360.
- [41] L. Macheli, G.M. Leteba, S.L. George, C.I. Lang, L.L. Jewell, Pt-based electrocatalysts for oxygen reduction reaction: Core-shell architectures and high-entropy alloy nanoparticles, *Adv. Energy Sustain. Res.* (2025) 2500201.
- [42] X. Zhao, K. Sasaki, Advanced Pt-based core-shell electrocatalysts for fuel cell cathodes, *Acc. Chem. Res.* 55 (9) (2022) 1226–1236.
- [43] M. Liu, H. Xin, Q. Wu, Unusual strain effect of a Pt-based L1 0 face-centered tetragonal core in core/shell nanoparticles for the oxygen reduction reaction, *Phys. Chem. Chem. Phys.* 21 (12) (2019) 6477–6484.
- [44] Z. Wang, X. Chen, T. Lin, B. Zhang, K. Song, L. Gu, T. Edvinsson, H. Liu, R.B. Araujo, X. Yu, Machine learning-guided design of L12-type Pt-based high-entropy intermetallic compound for electrocatalytic hydrogen evolution, *Adv. Mater.* e10424.
- [45] M. Cui, C. Yang, S. Hwang, M. Yang, S. Overa, Q. Dong, Y. Yao, A.H. Brozena, D.A. Cullen, M. Chi, et al., Multi-principal elemental intermetallic nanoparticles synthesized via a disorder-to-order transition, *Sci. Adv.* 8 (4) (2022) eabm4322.
- [46] Z. Jia, T. Yang, L. Sun, Y. Zhao, W. Li, J. Luan, F. Lyu, L.-C. Zhang, J.J. Krusic, J.-J. Kai, et al., A novel multiinary intermetallic as an active electrocatalyst for hydrogen evolution, *Adv. Mater.* 32 (21) (2020) 2000385.
- [47] G. Zhu, Y. Jiang, H. Yang, H. Wang, Y. Fang, L. Wang, M. Xie, P. Qiu, W. Luo, Constructing structurally ordered high-entropy alloy nanoparticles on nitrogen-rich mesoporous carbon nanosheets for high-performance oxygen reduction, *Adv. Mater.* 34 (15) (2022) 2110128.
- [48] K. Zhao, X. Li, D. Su, High-entropy alloy nanocatalysts for electrocatalysis, *Acta Phys. Chim. Sin* 37 (2009077) (2021) 10–3866.

- [49] Y. Ma, Y. Ma, Q. Wang, S. Schweidler, M. Botros, T. Fu, H. Hahn, T. Brezesinski, B. Breitung, High-entropy energy materials: challenges and new opportunities, *Energy & Environ. Sci.* 14 (5) (2021) 2883–2905.
- [50] Y. Yao, Q. Dong, A. Brozena, J. Luo, J. Miao, M. Chi, C. Wang, I.G. Kevrekidis, Z.J. Ren, J. Greeley, et al., High-entropy nanoparticles: Synthesis-structure-property relationships and data-driven discovery, *Science* 376 (6589) (2022) eabn3103.
- [51] T. Luan, J. Zhao, T. Gao, F. Wang, H. Xu, Z. Song, L. Luo, S. Gong, B. Liu, Efficient design of PtFeCoNiX ordered high-entropy alloys as multifunctional high-performance electrocatalysts, *Adv. Funct. Mater.* (2025) 2506851.
- [52] Z. Wang, Y. Gu, L. Zheng, J. Hou, H. Zheng, S. Sun, L. Wang, Machine learning guided dopant selection for metal oxide-based photoelectrochemical water splitting: the case study of Fe2O3 and CuO, *Adv. Mater.* 34 (10) (2022) 2106776.
- [53] H. Chun, E. Lee, K. Nam, J.-H. Jang, W. Kyoung, S.H. Noh, B. Han, First-principle-data-integrated machine-learning approach for high-throughput searching of ternary electrocatalyst toward oxygen reduction reaction, *Chem Catal.* 1 (4) (2021) 855–869.
- [54] Q. Gao, H.S. Pillai, Y. Huang, S. Liu, Q. Mu, X. Han, Z. Yan, H. Zhou, Q. He, H. Xin, et al., Breaking adsorption-energy scaling limitations of electrocatalytic nitrate reduction on intermetallic CuPd nanocubes by machine-learned insights, *Nat. Commun.* 13 (1) (2022) 2338.
- [55] N. Omidvar, S.-H. Wang, Y. Huang, H.S. Pillai, A. Athawale, S. Wang, L.E. Achenie, H. Xin, Explainable AI for optimizing oxygen reduction on Pt monolayer core-shell catalysts, *Electrochem. Sci. Adv.* 4 (6) (2024) e202300028.
- [56] B. Diao, C. Wang, R. Wang, Z. Feng, J. Zhang, H. Yang, Y. Tan, H. Wang, C. Wang, L. Liu, et al., Human kidney is a target for novel severe acute respiratory syndrome coronavirus 2 infection, *Nat. Commun.* 12 (1) (2021) 2506.
- [57] L. Zhang, X. Zhang, C. Chen, J. Zhang, W. Tan, Z. Xu, Z. Zhong, L. Du, H. Song, S. Liao, et al., Machine learning-aided discovery of low-Pt high entropy intermetallic compounds for electrochemical oxygen reduction reaction, *Angew. Chem.* 136 (51) (2024) e202411123.
- [58] Y. Pan, Y. Chen, Y. Li, M. Liu, L. Yao, H. Zhao, X. Zhao, Z. Yue, S. Gui, Y. Chen, et al., Entropy-increase assisted anti-sintering for synthesis of high-loaded Pt intermetallic compounds as electrocatalysts in PEMFCs, *Adv. Funct. Mater.* (2025) 2503628.
- [59] Y. Zeng, M. Zhao, Z. Huang, W. Zhu, J. Zheng, Q. Jiang, Z. Wang, H. Liang, Surface reconstruction of water splitting electrocatalysts, *Adv. Energy Mater.* 12 (33) (2022) 2201713.
- [60] Z. Wu, L. Huang, H. Liu, H. Wang, Element-specific restructuring of anion- and cation-substituted cobalt phosphide nanoparticles under electrochemical water-splitting conditions, *ACS Catal.* 9 (4) (2019) 2956–2961.
- [61] Y. Zhang, L. Gao, E.J. Hensen, J.P. Hofmann, Evaluating the stability of Co2P electrocatalysts in the hydrogen evolution reaction for both acidic and alkaline electrolytes, *ACS Energy Lett.* 3 (6) (2018) 1360–1365.
- [62] M. Cao, W. Li, T. Li, F. Zhu, X. Wang, Polymetallic amorphous materials: Research progress in synthetic strategies and electrocatalytic applications, *J. Mater. Chem. A* (2024).
- [63] Q. Fu, L.W. Wong, F. Zheng, X. Zheng, C.S. Tsang, K.H. Lai, W. Shen, T.H. Ly, Q. Deng, J. Zhao, Unraveling and leveraging in situ surface amorphization for enhanced hydrogen evolution reaction in alkaline media, *Nat. Commun.* 14 (1) (2023) 6462.
- [64] X. Zhang, J. Zhang, B. Xu, K. Wang, X.W. Sun, Synergistic effects in biphasic nanostructured electrocatalyst: Crystalline core versus amorphous shell, *Nano Energy* 41 (2017) 788–797.
- [65] Z. Lyu, J. Cai, X.-G. Zhang, H. Li, H. Huang, S. Wang, T. Li, Q. Wang, Z. Xie, S. Xie, Biphase Pd nanosheets with atomic-hybrid RhOx/Pd amorphous skins disentangle the activity-stability trade-off in oxygen reduction reaction, *Adv. Mater.* (2024) 2314252.
- [66] Z. Yu, Y. Chen, J. Xia, Q. Yao, Z. Hu, W.-H. Huang, C.-W. Pao, W. Hu, X.-M. Meng, L.-M. Yang, et al., Amorphization activated multimetallic Pd alloys for boosting oxygen reduction catalysis, *Nano Lett.* 24 (4) (2024) 1205–1213.
- [67] S.H. Noh, B. Han, T. Ohsaka, First-principles computational study of highly stable and active ternary PtCuNi nanocatalyst for oxygen reduction reaction, *Nano Res.* 8 (2015) 3394–3403.
- [68] L. Li, H. xin Ma, X. dong Jian, P. Qian, Y. jing Su, Degradation of the transition metal@ Pt core-shell nanoparticle catalyst: a DFT study, *Phys. Chem. Chem. Phys.* 22 (17) (2020) 9467–9476.
- [69] M.A. Matin, J. Lee, G.W. Kim, H.-U. Park, B.J. Cha, S. Shastri, G. Kim, Y.-D. Kim, Y.-U. Kwon, V. Petkov, Morphing mncore@ ptshell nanoparticles: Effects of core structure on the ORR performance of Pt shell, *Appl. Catal. B: Environ.* 267 (2020) 118727.
- [70] S. Gong, Y.-X. Zhang, Z. Niu, Recent advances in earth-abundant core/noble-metal shell nanoparticles for electrocatalysis, *ACS Catal.* 10 (19) (2020) 10886–10904.
- [71] A.S. Nair, B. Pathak, Computational screening for orr activity of 3d transition metal based m@ pt core-shell clusters, *J. Phys. Chem. C* 123 (6) (2019) 3634–3644.
- [72] A. Garg, M. Milina, M. Ball, D. Zanchet, S.T. Hunt, J.A. Dumesic, Y. Román-Leshkov, Transition-metal nitride core@ noble-metal shell nanoparticles as highly CO tolerant catalysts, *Angew. Chem. Int. Ed.* 56 (30) (2017) 8828–8833.
- [73] Z.-P. Wu, D.T. Caracciolo, Y. Maswadeh, J. Wen, Z. Kong, S. Shan, J.A. Vargas, S. Yan, E. Hopkins, K. Park, et al., Alloying–realloying enabled high durability for Pt–Pd–3d-transition metal nanoparticle fuel cell catalysts, *Nat. Commun.* 12 (1) (2021) 859.
- [74] X. Huang, G. Yang, S. Li, H. Wang, Y. Cao, F. Peng, H. Yu, Noble-metal-based high-entropy-alloy nanoparticles for electrocatalysis, *J. Energy Chem.* 68 (2022) 721–751.
- [75] H. Minamihara, K. Kusada, D. Wu, T. Yamamoto, T. Toriyama, S. Matsumura, L.S.R. Kumara, K. Ohara, O. Sakata, S. Kawaguchi, et al., Continuous-flow reactor synthesis for homogeneous 1 nm-sized extremely small high-entropy alloy nanoparticles, *J. Am. Chem. Soc.* 144 (26) (2022) 11525–11529.
- [76] H. Qi, F. Lu, Q. Li, Q. Wu, Z. Kang, Y. Hou, L. Su, S. Li, Z. Huang, G. Feng, Sub-5 nm ultrasmall high-entropy alloy nanomaterials for electrocatalysis, *Adv. Funct. Mater.* (2025) e19434.
- [77] S. Nellaappan, N.K. Katiyar, R. Kumar, A. Parui, K.D. Malviya, K. Pradeep, A.K. Singh, S. Sharma, C.S. Tiwary, K. Biswas, High-entropy alloys as catalysts for the CO2 and CO reduction reactions: experimental realization, *ACS Catal.* 10 (6) (2020) 3658–3663.
- [78] D. Wu, K. Kusada, T. Yamamoto, T. Toriyama, S. Matsumura, I. Gueye, O. Seo, J. Kim, S. Hiroi, O. Sakata, et al., On the electronic structure and hydrogen evolution reaction activity of platinum group metal-based high-entropy-alloy nanoparticles, *Chem. Sci.* 11 (47) (2020) 12731–12736.
- [79] M. Liu, Z. Zhang, F. Okejiri, S. Yang, S. Zhou, S. Dai, Entropy-maximized synthesis of multimetallic nanoparticle catalysts via a ultrasonication-assisted wet chemistry method under ambient conditions, *Adv. Mater. Interfaces* 6 (7) (2019) 1900015.
- [80] L. Banko, O.A. Krysiak, J.K. Pedersen, B. Xiao, A. Savan, T. Löfller, S. Baha, J. Rossmeisl, W. Schuhmann, A. Ludwig, Unravelling composition-activity-stability trends in high entropy alloy electrocatalysts by using a data-guided combinatorial synthesis strategy and computational modeling, *Adv. Energy Mater.* 12 (8) (2022) 2103312.
- [81] Z. Wu, G. Yang, Z. Liu, S. Du, Q. Zhang, F. Peng, Explosive leidenfrost-droplet-mediated synthesis of monodispersed high-entropy-alloy nanoparticles for electrocatalysis, *Nano Lett.* 24 (24) (2024) 7158–7165.
- [82] X. Huang, Z. Wu, B. Zhang, G. Yang, H.-F. Wang, H. Wang, Y. Cao, F. Peng, S. Li, H. Yu, Formation of disordered high-entropy-alloy nanoparticles for highly efficient hydrogen electrocatalysis, *Small* 20 (29) (2024) 2311631.
- [83] Z.-X. Cai, S. Bolar, Y. Ito, T. Fujita, Enhancing oxygen evolution reactions in nanoporous high-entropy catalysts using boron and phosphorus additives, *Nanoscale* 16 (9) (2024) 4803–4810.
- [84] G. Lee, N.-A. Nguyen, V.-T. Nguyen, L.L. Larina, E. Chuluunbat, E. Park, J. Kim, H.-S. Choi, M. Keidar, High entropy alloy electrocatalyst synthesized using plasma ionic liquid reduction, *J. Solid State Chem.* 314 (2022) 123388.
- [85] Q. Wang, Y. Qin, J. Xie, Y. Kong, Q. Sun, Z. Wei, S. Zhao, Size-controllable high-entropy alloys toward stable hydrogen production at industrial-scale current densities, *Adv. Mater.* 37 (10) (2025) 2420173.
- [86] E.B. Tetteh, O.A. Krysiak, A. Savan, M. Kim, R. Zerdoumi, T.D. Chung, A. Ludwig, W. Schuhmann, Long-range SECCM enables high-throughput electrochemical screening of high entropy alloy electrocatalysts at up-to-industrial current densities, *Small Methods* 8 (7) (2024) 2301284.
- [87] M.K. Plenge, J.K. Pedersen, L.A. Cipriano, J. Rossmeisl, Electrochemical dissolution: Paths in high-entropy alloy composition space, *High Entropy Alloy. Mater.* (2025) 1–13.
- [88] M.K. Plenge, J.K. Pedersen, V.A. Mints, M. Arenz, J. Rossmeisl, Following paths of maximum catalytic activity in the composition space of high-entropy alloys, *Adv. Energy Mater.* 13 (2) (2023) 2202962.
- [89] J.K. Pedersen, T.A. Batchelor, D. Yan, L.E.J. Skjegstad, J. Rossmeisl, Surface electrocatalysis on high-entropy alloys, *Curr. Opin. Electrochem.* 26 (2021) 100651.
- [90] L. Huang, Z. Gariepy, E. Halpren, L. Du, C.H. Shan, C. Yang, Z.W. Chen, C.V. Singh, Bayesian learning aided theoretical optimization of IrPdPtRhRu high entropy alloy catalysts for the hydrogen evolution reaction, *Small Methods* 9 (5) (2025) 2401224.
- [91] S. Bolar, Y. Ito, T. Fujita, Future prospects of high-entropy alloys as next-generation industrial electrode materials, *Chem. Sci.* 15 (23) (2024) 8664–8722.
- [92] P. Zhang, X. Hui, Y. Nie, R. Wang, C. Wang, Z. Zhang, L. Yin, New conceptual catalyst on spatial high-entropy alloy heterostructures for high-performance Li-O2 batteries, *Small* 19 (15) (2023) 2206742.
- [93] W. Shi, H. Liu, Z. Li, C. Li, J. Zhou, Y. Yuan, F. Jiang, K. Fu, Y. Yao, High-entropy alloy stabilized and activated Pt clusters for highly efficient electrocatalysis, *SusMat* 2 (2) (2022) 186–196.
- [94] L. Li, M. Hua, J. Li, P. Zhang, Y. Nie, P. Wang, X. Lin, Z. Zhang, R. Wang, X. Ge, et al., Tuning dual catalytic active sites of Pt single atoms paired with high-entropy alloy nanoparticles for advanced Li-O2 batteries, *ACS Nano* 19 (4) (2025) 4391–4402.
- [95] X. Zhao, H. Cheng, X. Chen, Q. Zhang, C. Li, J. Xie, N. Marinkovic, L. Ma, J.-C. Zheng, K. Sasaki, Multiple metal–nitrogen bonds synergistically boosting the activity and durability of high-entropy alloy electrocatalysts, *J. Am. Chem. Soc.* 146 (5) (2024) 3010–3022.

- [96] L.J. Sham, W. Kohn, One-particle properties of an inhomogeneous interacting electron gas, *Phys. Rev.* 145 (2) (1966) 561.
- [97] P. Hohenberg, W. Kohn, Inhomogeneous electron gas, *Phys. Rev.* 136 (3B) (1964) B864.
- [98] B. Hammer, L.B. Hansen, J.K. Nørskov, Improved adsorption energetics within density-functional theory using revised Perdew-Burke-Ernzerhof functionals, *Phys. Rev. B* 59 (11) (1999) 7413.
- [99] G. Kresse, J. Hafner, Norm-conserving and ultrasoft pseudopotentials for first-row and transition elements, *J. Phys.: Condens. Matter.* 6 (40) (1994) 8245.
- [100] G. Kresse, J. Hafner, Ab initio molecular-dynamics simulation of the liquid-metal-amorphous-semiconductor transition in germanium, *Phys. Rev. B* 49 (20) (1994) 14251.
- [101] G. Kresse, J. Furthmüller, Efficient iterative schemes for ab initio total-energy calculations using a plane-wave basis set, *Phys. Rev. B* 54 (16) (1996) 11169.
- [102] P.E. Blöchl, Projector augmented-wave method, *Phys. Rev. B* 50 (24) (1994) 17953.
- [103] S. Grimme, J. Antony, S. Ehrlich, H. Krieg, A consistent and accurate ab initio parametrization of density functional dispersion correction (DFT-D) for the 94 elements H-Pu, *J. Chem. Phys.* 132 (15) (2010) 154104.
- [104] A. Stukowski, Visualization and analysis of atomistic simulation data with OVITO—the open visualization tool, *Modelling Simul. Mater. Sci. Eng.* 18 (1) (2009) 015012.
- [105] K. Momma, F. Izumi, VESTA: a three-dimensional visualization system for electronic and structural analysis, *J. Appl. Crystallogr.* 41 (3) (2008) 653–658.
- [106] K. Momma, F. Izumi, VESTA 3 for three-dimensional visualization of crystal, volumetric and morphology data, *J. Appl. Crystallogr.* 44 (6) (2011) 1272–1276.
- [107] W. Tang, E. Sanville, G. Henkelman, A grid-based Bader analysis algorithm without lattice bias, *J. Phys.: Condens. Matter.* 21 (8) (2009) 084204.
- [108] R. Ferrando, G. Rossi, A.C. Levi, Z. Kuntová, F. Nita, A. Jelea, C. Mottet, G. Barcaro, A. Fortunelli, J. Goniakowski, Structures of metal nanoparticles adsorbed on MgO (001). I. Ag and Au, *J. Chem. Phys.* 130 (17) (2009).
- [109] M.T. Ruggiero, A. Erba, R. Orlando, T.M. Korter, Origins of contrasting copper coordination geometries in crystalline copper sulfate pentahydrate, *Phys. Chem. Chem. Phys.* 17 (46) (2015) 31023–31029.
- [110] V.L. Deringer, A.L. Tchougréeff, R. Dronkowski, Crystal orbital hamilton population (COHP) analysis as projected from plane-wave basis sets, *J. Phys. Chem. A* 115 (21) (2011) 5461–5466.
- [111] B. Hammer, J.K. Nørskov, Theoretical surface science and catalysis—calculations and concepts, in: *Advances in Catalysis*, vol. 45, Elsevier, 2000, pp. 71–129.
- [112] S. Zha, Z.-J. Zhao, S. Chen, S. Liu, T. Liu, F. Studt, J. Gong, Predicting the catalytic activity of surface oxidation reactions by ionization energies, *CCS Chem.* 2 (4) (2020) 262–270.
- [113] F. Calle-Vallejo, J.I. Martínez, J.M. García-Lastra, P. Sautet, D. Loffreda, Fast prediction of adsorption properties for platinum nanocatalysts with generalized coordination numbers, *Angew. Chem. Int. Ed.* 53 (32) (2014) 8316–8319.
- [114] S. Jiao, X. Fu, H. Huang, Descriptors for the evaluation of electrocatalytic reactions: d-band theory and beyond, *Adv. Funct. Mater.* 32 (4) (2022) 2107651.
- [115] A.A. Mikhailova, A.P. Maltsev, P.C. Mendes, F.B. Zamudio, A.R. Oganov, S.M. Kozlov, Structure and adsorption properties of Cu–Au nanoparticles in harsh reactive environments, *J. Chem. Phys.* 163 (12) (2025).
- [116] A.A. Mikhailova, S.V. Lepeshkin, V.S. Baturin, A.P. Maltsev, Y.A. Uspenskii, A.R. Oganov, Ultralow reaction barriers for CO oxidation in Cu–Au nanoclusters, *Nanoscale* 15 (33) (2023) 13699–13707.
- [117] X.-N. Li, Z. Yuan, S.-G. He, CO oxidation promoted by gold atoms supported on titanium oxide cluster anions, *J. Am. Chem. Soc.* 136 (9) (2014) 3617–3623.
- [118] J.-J. Chen, X.-N. Li, Q. Chen, Q.-Y. Liu, L.-X. Jiang, S.-G. He, Neutral Au1-doped cluster catalysts AuTi2O3–6 for CO oxidation by O<sub>2</sub>, *J. Am. Chem. Soc.* 141 (5) (2018) 2027–2034.
- [119] A.D. Radina, V.S. Baidyshev, I.V. Chepkasov, N.A. Matsokin, T. Altalhi, B.I. Yakobson, A.G. Kvashnin, Theoretical study of adsorption properties and CO oxidation reaction on surfaces of higher tungsten boride, *Sci. Rep.* 14 (1) (2024) 12788.
- [120] M.A. Dar, S. Krishnamurti, Molecular and dissociative adsorption of oxygen on Au–Pd bimetallic clusters: Role of composition and spin state of the cluster, *ACS Omega* 4 (7) (2019) 12687–12695.
- [121] I.V. Chepkasov, V.S. Baidyshev, A.V. Iosimovska, I.S. Zamulin, A.G. Kvashnin, Adsorption properties of crystalline and amorphous PdIr nanoparticles. a systematic first-principles study, *J. Catalysis* 447 (2025) 116102.
- [122] Q. Guan, C. Zhu, Y. Lin, E.I. Vovk, X. Zhou, Y. Yang, H. Yu, L. Cao, H. Wang, X. Zhang, et al., Bimetallic monolayer catalyst breaks the activity–selectivity trade-off on metal particle size for efficient chemoselective hydrogenations, *Nat. Catal.* 4 (10) (2021) 840–849.
- [123] X. Zhang, Z. Sun, R. Jin, C. Zhu, C. Zhao, Y. Lin, Q. Guan, L. Cao, H. Wang, S. Li, et al., Conjugated dual size effect of core-shell particles synergizes bimetallic catalysis, *Nat. Commun.* 14 (1) (2023) 530.
- [124] J.P. Carbone, A. Irmler, A. Gallo, T. Schäfer, W.Z. Van Benschoten, J.J. Shepherd, A. Grüneis, CO adsorption on Pt (111) studied by periodic coupled cluster theory, *Faraday Discuss.* 254 (2024) 586–597.
- [125] Y. Nanba, M. Koyama, NO adsorption on 4d and 5d transition-metal (Rh, Pd, Ag, Ir, and Pt) nanoparticles: density functional theory study and supervised learning, *J. Phys. Chem. C* 123 (46) (2019) 28114–28122.
- [126] J. Chen, M. Aliaggar, F.B. Zamudio, T. Zhang, Y. Zhao, X. Lian, L. Wen, H. Yang, W. Sun, S.M. Kozlov, et al., Diversity of platinum-sites at platinum/fullerene interface accelerates alkaline hydrogen evolution, *Nat. Commun.* 14 (1) (2023) 1711.
- [127] Y.-C. Hsiao, C.-Y. Wu, C.-H. Lee, W.-Y. Huang, H.V. Thang, C.-C. Chi, W.-J. Zeng, J.-Q. Gao, C.-Y. Lin, J.-T. Lin, et al., A library of seed@ high-entropy-alloy core-shell nanocrystals with controlled facets for catalysis, *Adv. Mater.* 37 (6) (2025) 241146.
- [128] G.R. Dey, H.L. Young, S. Teklu, S.S. Soliman, R.E. Schaak, Influence of nanoparticle seeds on the formation and growth of high entropy alloys during core@ shell nanoparticle synthesis, *ACS Nano* 19 (9) (2025) 8826–8841.
- [129] Y.-H. Liu, C.-J. Hsieh, L.-C. Hsu, K.-H. Lin, Y.-C. Hsiao, C.-C. Chi, J.-T. Lin, C.-W. Chang, S.-C. Lin, C.-Y. Wu, et al., Toward controllable and predictable synthesis of high-entropy alloy nanocrystals, *Sci. Adv.* 9 (19) (2023) eadff9931.
- [130] F. Abild-Pedersen, J. Greeley, F. Studt, J. Rossmeisl, T.R. Munter, P.G. Moses, E. Skulason, T. Bligaard, J.K. Nørskov, Scaling properties of adsorption energies for hydrogen-containing molecules<? format?> on transition-metal surfaces, *Phys. Rev. Lett.* 99 (1) (2007) 016105.
- [131] E.M. Fernández, P.G. Moses, A. Toftlund, H.A. Hansen, J.I. Martínez, F. Abild-Pedersen, J. Kleis, B. Hinnemann, J. Rossmeisl, T. Bligaard, et al., Scaling relationships for adsorption energies on transition metal oxide, sulfide, and nitride surfaces, *Angew. Chem. Int. Ed.* 47 (25) (2008) 4683–4686.
- [132] S. Pablo-García, S. Morandi, R.A. Vargas-Hernández, K. Jorner, Ž. Ivković, N. López, A. Aspuru-Guzik, Fast evaluation of the adsorption energy of organic molecules on metals via graph neural networks, *Nat. Comput. Sci.* 3 (5) (2023) 433–442.
- [133] X. Li, R. Chiong, Z. Hu, A.J. Page, A graph neural network model with local environment pooling for predicting adsorption energies, *Comput. Theor. Chem.* 1226 (2023) 114161.
- [134] X. Lin, X. Du, S. Wu, S. Zhen, W. Liu, C. Pei, P. Zhang, Z.-J. Zhao, J. Gong, Machine learning-assisted dual-atom sites design with interpretable descriptors unifying electrocatalytic reactions, *Nat. Commun.* 15 (1) (2024) 8169.
- [135] Z. Song, X. Wang, F. Liu, Q. Zhou, W.-J. Yin, H. Wu, W. Deng, J. Wang, Distilling universal activity descriptors for perovskite catalysts from multiple data sources via multi-task symbolic regression, *Mater. Horizons* 10 (5) (2023) 1651–1660.
- [136] T. Shiota, K. Ishihara, W. Mizukami, Lowering the exponential wall: accelerating high-entropy alloy catalysts screening using local surface energy descriptors from neural network potentials, *Digit. Discov.* 4 (3) (2025) 738–751.
- [137] C. Cai, T. Wang, Resolving chemical-motif similarity with enhanced atomic structure representations for accurately predicting descriptors at metallic interfaces, *Nat. Commun.* 16 (1) (2025) 8761.
- [138] Q. Wang, Y. Yao, Harnessing machine learning for high-entropy alloy catalysis: a focus on adsorption energy prediction, *Npj Comput. Mater.* 11 (1) (2025) 91.
- [139] C. Wang, B. Wang, C. Wang, A. Li, Z. Chang, R. Wang, A machine learning model with minimize feature parameters for multi-type hydrogen evolution catalyst prediction, *Npj Comput. Mater.* 11 (1) (2025) 111.